

Small-Scale air turbulence structure, microphysical time scales and local supersaturation balance at a warm Cloud Top Boundary

Ludovico Fossà,^{a)} Shahbozbek Abdunabiev, Mina Golshan, and Daniela Tordella
*Dipartimento di Scienza Applicata e Tecnologia, Politecnico di Torino,
Italy*

(*Electronic mail: daniela.tordella@polito.it)

(Dated: 8 March 2022)

Recent results have shown that there is an acceleration in the spread of the size distribution of droplet populations in the region bordering the cloud and undersaturated ambient. We have analyzed the supersaturation balance in this region, which is typically a highly intermittent shearless turbulent mixing layer, under a condition where there is no mean updraft. We have investigated the evolution of the cloud-clear air interface and of the droplets therein via direct numerical simulations. We have compared horizontal averages of the phase relaxation, evaporation, reaction and condensation times within the cloud-clear air interface for the size distributions of the initial monodisperse and polydisperse droplets. For the monodisperse population, a clustering of the values of the reaction, phase and evaporation times, that is around 20-30 seconds, is observed in the central area of the mixing layer, just before the location where the maximum value of the supersaturation turbulent flux occurs. This clustering of values is similar for the polydisperse population but also includes the condensation time. The mismatch between the time derivative of the supersaturation and the condensation term in the interfacial mixing layer is correlated with the planar covariance of the horizontal longitudinal velocity derivatives of the carrier air flow and the supersaturation field, thus suggesting that a quasi-linear relationship may exist between these quantities.

^{a)}Present address: Department of Mechanical engineering, the University of Sheffield, the United Kingdom.

I. INTRODUCTION

The large-scale dynamics of warm atmospheric clouds is closely coupled with small-scale phenomena. Lukewarm clouds are a stage of a complex interplay between competing turbulent and microphysical processes, which determine their evolution over time. However, many physical processes that are relevant for cloud dynamics have not yet been completely unravelled, and still constitute a matter of debate in the cloud physics and turbulence communities. In recent years, a great deal of attention has been paid to the effect of turbulent mixing at cloud boundaries as well as its impact on droplet condensation (evaporation) and collision. The interfacial mixing of cloud and clear air has often been identified as the main cause of the observed broadening of droplet size distributions and the rapid onset of precipitation.

Warner (1969)¹ suggested the importance of mixing at a growing cloud top in unstable environments. Latham and Reed (1977)² and Baker, Corbin and Latham (1980)³ were the first to recognize a difference between homogeneous and inhomogeneous mixing, where the microphysics time scale can be either longer or shorter than the time scale of the turbulent motions. The ratio between the turbulent time scale and the microphysical time scale is represented by the Damköhler number, Da . The same turbulent flow encompasses a wide range of Da along the energy cascade⁴. Several time scales have been used to define the Damköhler number⁵, and to parameterize the impact of the entrainment and mixing of clear air at cloud boundaries. These scales include evaporation, phase relaxation and reaction time scales. The fundamental variable that drives the condensation (evaporation) of a droplet is supersaturation $S = RH - 1$, where RH is the relative humidity⁶. S varies over both time and space, and is determined by the local, instantaneous concentration of water vapor ρ_v and temperature T through the Clausius-Clapeyron equation. However, supersaturation S has often been described as a somewhat global property of a cloud parcel⁷, and the local value of the vertical velocity and the microphysical properties are generally taken into account for its estimation. The supersaturation balance within a cloud is often described by means of a production-condensation model of the type proposed by⁸, where the mean updraft velocity w and the mean radius of the droplet population \bar{R} are the main contributors to the time derivative of S

$$\frac{dS}{dt} \cong c_1 w - \frac{S}{\tau_{phase}} \quad (1)$$

where $\tau_{phase} = (c_2 n_d \bar{R})^{-1}$ is the phase relaxation timescale^{9,10}, n_d is the droplet number density and c_1, c_2 are coefficients that depend, albeit only slightly, on the temperature, c_1 and temperature/pressure, c_2 ,¹¹. Cooper (1989)¹² described a theoretical framework in which the variability of S , and the subsequent broadening of the droplet size distribution are determined by the value of the integral radius as well as by the covariance of the integral radius and the vertical velocity fluctuation.

Sardina et al. 2015 generalized Twomey's model to a scalar transport equation that they used in their direct numerical simulation (DNS) study of cloud cores¹³. They showed that the contribution of the diffusive effect is negligible for large Reynolds numbers. Chandrakar et al. (2016)¹⁴, in a

laboratory experiment, used the stochastic condensation model of¹³ to investigate the effects of an aerosol concentration on the broadening of the droplet size distribution. They argued that supersaturation fluctuations determine diverse growth conditions inside cloud cores with low aerosol (and droplet) concentrations.¹⁵, who studied the impact of turbulent temperature and water vapor density fluctuations on supersaturation by performing in-situ measurements of shallow-cumulus clouds, suggested the same. Their data show a reduction in the standard deviation of supersaturation inside cloud cores compared to regions where few or no droplets are located. They used the phase relaxation time τ_{phase} as the microphysical time scale in the Damköhler number. Prabhakaran (2020)¹⁶ used the stochastic condensation approach to study the activation of dry-sodium chloride aerosols, as well as droplet nucleation and growth via laboratory experiments. They used a climate chamber where statistically steady-state Rayleigh-Bénard turbulence had been generated. They claimed that their results can be extended to a context in which the effects of entrainment and mixing are important, and that, in this case, droplet activation is governed by a fluctuation-dominated regime, even though such a region is subsaturated on the whole.

However, many DNS studies have focused on both statistically steady-state and transient shearless mixing layers located at a vertical droplet-laden, cloud-clear air interface^{17,18}. Kumar et al.(2018)¹⁹ investigated the effects of the range of the energy cascade on the relative dispersion of a droplet population, which was observed to increase for larger initial values of the domain size-based Da. Miller and Bellan (2000)²⁰ performed direct numerical simulations (DNS) of a droplet-laden shear layer that featured a two-way interphase coupling and a Lagrangian tracking system for the droplets. Onishi, Takahashi and Komori (2009)²¹ studied the influence of gravity on droplet collision and coalescence. Sidin, Ijzermans and Reeds (2009)²² used a synthetic turbulent field to investigate the impact of both large and small-scale turbulent eddies on droplet condensation and evaporation. Their DNS model did not take into account the effects of condensation and evaporation. Recently, Golshan et al. (2021)²³ have recently performed direct numerical simulations of a horizontal, droplet-laden, interfacial shearless mixing layer subject to unstable stratification. They observed a remarkable acceleration in the dynamics of the droplet population in the mixing layer, in particular in the temporal evolution of the droplet collision/evaporation rates and in their spectrum broadening. These findings were linked to the large intermittency of the small-scale turbulence, which is driven by the anisotropy of the carrier flow shearless layer and by the active scalars transported there.

The aim of the present work is twofold: first, to compute and compare the various microphysical time scales in the cloudy - clear air interfacial layer so far proposed in the literature, second, to infer a possible source term for Twomey's equation (1) that accounts for the small-scale statistics of the carrier flow at a cloud-top boundary where the updraft is null. We have used the dataset computed from the aforementioned direct numerical simulation campaign performed by²³. We have adopted a high-resolution pseudospectral method that allows us to observe the temporal evolution of the supersaturation fluctuations and the velocity derivative statistics across the horizontal turbulent shearless mixing layer (for the gas phase dynamics, see²⁴).

The physical model of a shearless cloud-clear air interface, together with the relevant governing equations of the direct numerical simulations, are presented in section II. The obtained results are discussed in section III, and the conclusions are drawn in section IV.

II. PHYSICAL PROBLEM AND MATHEMATICAL FRAMEWORK

A. Physical model and governing equations

The aim here has been to study the transient decay of a top cloud-clear air interface by performing direct numerical simulations of a turbulent shearless mixing layer. This idealized interfacial layer separates two regions. A warmer, droplet-laden cloud region is located at the bottom half of the domain and it is rich in water vapor and kinetic energy. A clear air less energetic area lies in the top half of the computational domain, which is a parallelepiped made up of two adjacent cubes, see Fig. 1, panels a and b.

A turbulent layer without mean shear is a reasonable model of turbulence at the boundary between atmospheric clouds and the surrounding undersaturated air. This flow is considered simple because it is free of the complications associated with the production of turbulence due to the mean flow. However, in reality it is home to dynamic aspects that are not obvious and have not yet been fully described or understood. We briefly list some of them hereafter. To form a shear-free turbulent layer, it is sufficient that two contiguous non-sheared regions with a different integral scale and the same kinetic initial energy interact. This, in time, can generate a shear-free layer that hosts a gradient of kinetic energy²⁵. All the shear-free turbulent layers are in-homogeneous, thus anisotropic, and also intermittent at the small scale level. Anisotropy appears in the main diagonal of the velocity fluctuation gradient, which is characterised by a substantial absence of significant off-diagonal terms^{24,26}. The growth or reduction of the thickness of the layer is controlled to a great extent by the concomitant action of the local kinetic energy and spatial macroscale gradients. If these gradients have opposite signs across the layer, the thickening of the layer decelerates, and vice versa, if the signs are concordant²⁷. If the layers are stratified in density, substrates are formed. In the case of stable stratification, the energy collapses below the two formation region levels. Flow transport across the layer is blocked. In the case of unstable stratification, the sublayer hosts an accumulation of energy, and transport is enhanced²⁸.

Moreover, it should be noted that for the case where the most energetic portion beside the layer (cloud region) hosts both supersaturated water vapor and water droplets, recent results have shown that i) the small-scale intermittency of the air flow in the mixing layer is highly correlated with the drop collision rate of both the monodisperse and polydisperse drop size distributions, ii) a more intense widening of the drop population size spectrum is observed in the interfacial region with respect to what happens inside the homogeneous cloud region. These results have prompted our interest in exploring the correlation between supersaturation fluctuations and the small-scale intermittency of air flow turbulence. A relationship has here been hypothesized to be responsible for the so-called bottleneck problem associated with the interaction of the evaporation-condensation-

coalescence processes present in the formation of cumulus rain.

Boussinesq Navier-Stokes equations provide the Eulerian description of the incompressible, stratified, velocity fluctuation, u_i , along with active scalar transport equations for temperature, T , and water vapor density ρ_v ^{4,17–19,29–31}

$$\frac{\partial u_j}{\partial x_j} = 0 \quad (2a)$$

$$\frac{\partial u_i}{\partial t} + u_j \frac{\partial u_i}{\partial x_j} = -\frac{1}{\rho_0} \frac{\partial p}{\partial x_i} + \nu \frac{\partial^2 u_i}{\partial x_j^2} + \mathcal{B} \delta_{3i} \quad (2b)$$

$$\frac{\partial T}{\partial t} + u_j \frac{\partial T}{\partial x_j} = \kappa \frac{\partial^2 T}{\partial x_j^2} + \frac{\mathcal{L} C_d}{\rho_0 c_p} \quad (2c)$$

$$\frac{\partial \rho_v}{\partial t} + u_j \frac{\partial \rho_v}{\partial x_j} = \kappa_v \frac{\partial^2 \rho_v}{\partial x_j^2} - C_d \quad (2d)$$

where ρ_0 is the Boussinesq density (that is, the mean density of dry air 1000 m above the sea level), ν is the kinematic viscosity of the air, κ is the heat diffusivity of the air and κ_v the mass diffusivity of the water vapor. \mathcal{L} is the latent heat of evaporation of the water and c_p is the specific heat of the air at the mean domain temperature T_0 . All the physical constants in equations (2, a-d) are summarized in Table I. The Boussinesq approximation allows us to take into account small perturbations of a parcel density of moist air due to local temperature and vapor density variations³². The buoyancy term, \mathcal{B} , in equation (2b) can be expressed as a function of the local values of T and ρ_v

$$\mathcal{B} = g \left[\frac{\Delta T}{T_0} - \frac{\Delta \rho_v}{\rho_0} \left(1 - \frac{\mathcal{M}_a}{\mathcal{M}_w} \right) \right] \quad (3)$$

where \mathcal{M}_a and \mathcal{M}_w are the molar masses of the air and water, respectively. We adopt periodic boundary conditions for the velocity and water vapor density fields in the three directions. The temperature field is non-periodic in the vertical direction and results from the superposition of a triply-periodic scalar field and a constant, negative, vertical temperature gradient. The temperature of the cloud region being higher than the clear-air one, the interfacial mixing layer is subject to an unstable stratification with a squared Froude number, Fr_{int}^2 , approximately equal to -7 . This leads to a local increase in the momentum and kinetic energy, as a result of the Boussinesq body-force term in equation (2b).

The condensation term $C_d = C_d(x_i, t)$ in the energy and vapor density equation expresses the water vapor mass absorption (depletion) rate at the surface of all the spherical droplets contained in the cubic computational cell of volume $(\Delta)^3$ ²⁹. Since cloud droplets are advected by the turbulent flow, C_d must be determined in the Lagrangian reference frame used for the liquid water mixing ratio, which is described below in sub-section **II B**. However, in order to use C_d , in equations (2c) and (2d), it should be represented in the Eulerian frame of reference. The condensation rate field is determined as:

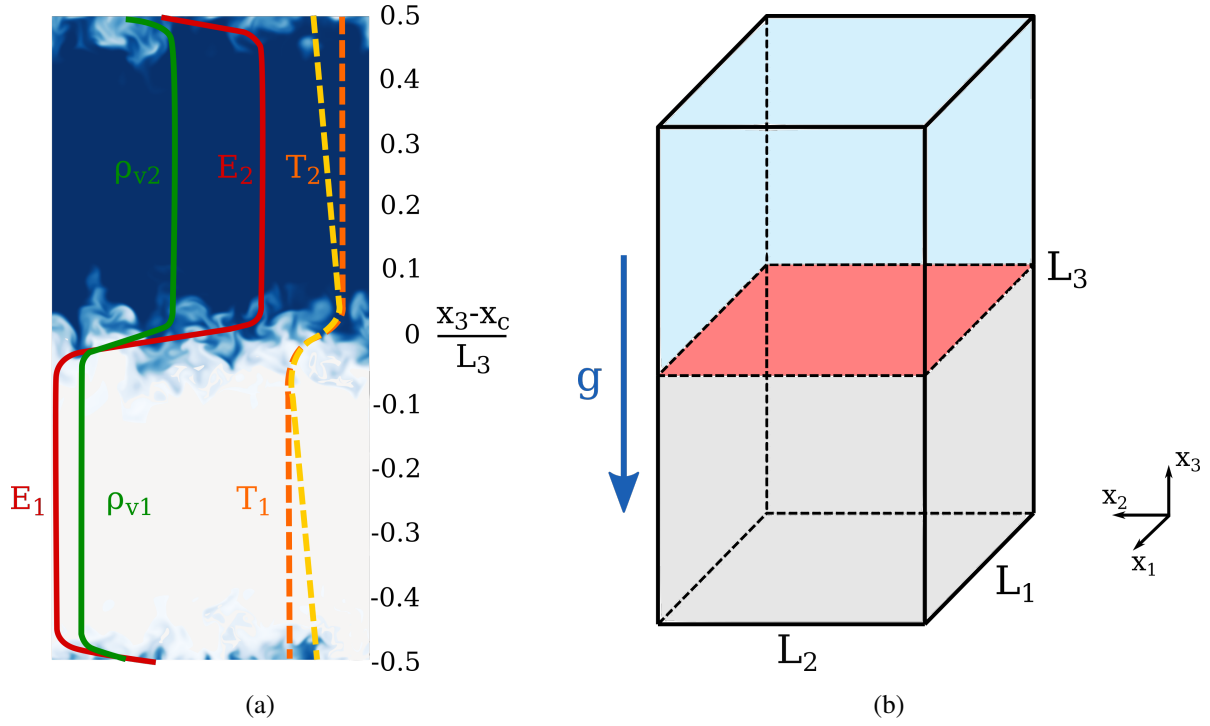


FIG. 1: Panel (a): initial distributions of kinetic energy E (solid dark red line), water vapor density ρ_v (solid green line) and temperature T (orange and yellow dash-dotted lines) in the vertical direction across the interfacial mixing layer. The mixing layer is located at $x_c = L_{12}$ (see Table II). The temperature fluctuation component $T'(x_3)$ of equation (11) is plotted with yellow the dash-dotted line, while the non-periodic physical temperature T is plotted with the orange dash-dotted line. Subscripts 1 and 2 refer to cloud and clear-air conditions (see Table I). Panel (b): The computational domain is a parallelepiped composed of two adjacent cubes. The total height L_3 is twice $L_{1,2}$. Subscripts 1 and 2 refer to the horizontal directions parallel to the mixing layer, whereas subscript 3 indicates the vertical direction.

$$C_d = \frac{1}{\Delta x^3} \frac{dm_w}{dt} = \frac{4\pi\rho_w}{\Delta x^3} \sum_{j=1}^{N_\Delta} R_j^2(\mathbf{X}_j(t)) \frac{dR_j(\mathbf{X}_j(t))}{dt} \quad (4)$$

where $R_j(t)$ and $\mathbf{X}_j(t)$ are the radius and the coordinate of the j -th drop contained within the grid cell, respectively, and N_Δ represents the number of drops inside each grid cell. The interpolation of Eulerian field values at grid points to the positions occupied by the water droplets inside the cell is obtained via second-order Lagrange polynomials. An inverse procedure is used to calculate the condensation rate, which is determined at the first step at each droplet position and then relocated to the closest of the eight grid vertices. The time derivative, dR_j/dt , expresses the droplet condensational shrinkage (growth) rate, as defined in Equation (8).

B. Lagrangian droplet dynamics and droplet populations

The Lagrangian motion of each k -th droplet in the physical system is modeled by a tracker of the type^{29,33}:

$$\frac{dX_{ki}}{dt} = V_{ki} \quad (5a)$$

$$\frac{dV_{ki}}{dt} = \frac{1}{\tau_k} [u_i(X_{ki}, t) - V_{ki}] + g\delta_{i3} \left(1 - \frac{\rho_0}{\rho_w}\right) \quad (5b)$$

which features two vector equations for position, X_{ki} , and velocity, V_{ki} , of a droplet within the reference frame, where i indicates the direction. The momentum equation is derived for low-Reynolds spherical droplets (e.g.^{29,31}) and only accounts for the contribution of Stokes' drag and gravity, while the effects of Faxen and Basset's history force are negligible^{23,31,34}. The inertia of a spherical droplet is proportional to its surface and is often expressed through a characteristic time scale, that is, the droplet response time (τ_d) of the k -th droplet with radius R_k ¹⁰

$$\tau_{dk} = \frac{2}{9} \frac{\rho_w R_k^2}{\rho_0 \nu} \quad (6)$$

which is also the time constant of the solution to equation (5b) for a steady, homogeneous flow.

It should be noted that, in a similar way to what is done for the condensation rate field, Eulerian flow field quantities have to be determined at the droplet position to numerically proceed with Lagrangian equations. In this context, we adopted a simplified feedback on the droplet flow. The direct effect of the liquid droplet drag on the velocity field is neglected in the buoyancy term in the momentum equation. The feedback is therefore indirect and is confined to the coupling of the temperature field with the velocity field and the vapour mixing ratio through the condensation rate. The rationale behind this position depends on the smallness Stokes' numbers of the drops and liquid mass and volume fractions $\sim 10^{-3}$ and $\sim 10^{-6}$, respectively. In fact, for radii in the range $[1 - 30]\mu\text{m}$, the initial transient values of Stokes' numbers are in $[0.02 - 0.7]$, while the end of transient values are in $[0.002 - 0.066]$, which means Reynolds numbers of the drops much lower than 1.

Spherical cloud droplets are assumed to collide and coalesce with full collision and coalescence efficiency whenever their relative distance falls below the sum of the respective radii

$$\left[\sum_{i=1}^3 (X_{li} - X_{ki})^2 \right]^{1/2} \leq R_l + R_k$$

The single droplet resulting from coalescence conserves the total mass and momentum of the colliding drops.

Both monodisperse and polydisperse droplet size distributions are considered in the present simulation campaign (Fig. 2). At the beginning of the simulation, the droplets are randomly distributed in the cloud region of the computational domain, where the clear air region is initially

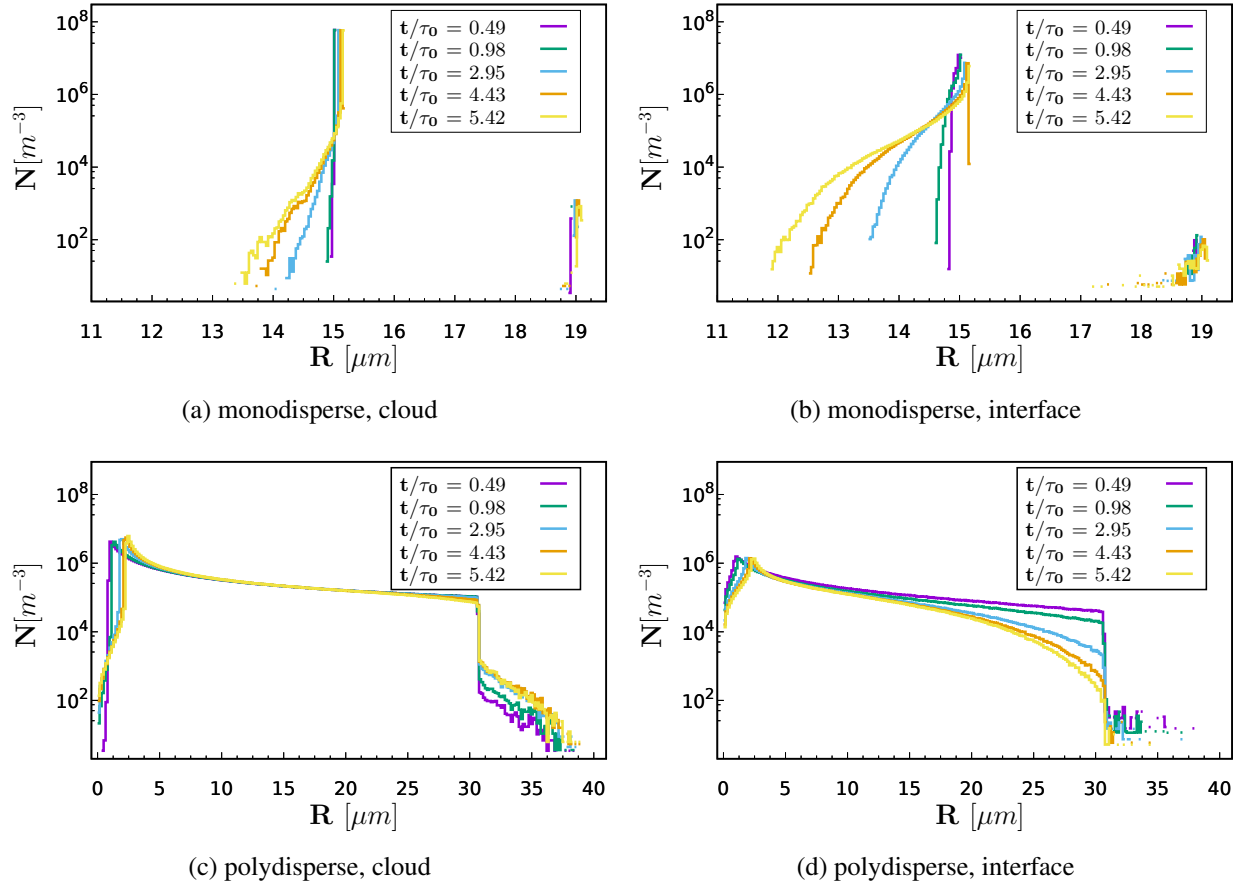


FIG. 2: Droplet size distributions as a function of the radius classes. Panels (a) and (b): size distribution for a monodisperse population ($R = 15 \mu\text{m}$) in the cloud and interface regions, respectively. Panels (c) and (d): size distribution for a polydisperse (equal mass in the droplet volume classes, $R \in [0.6 - 30] \mu\text{m}$) population in the cloud and interface regions, respectively.

void. The number of droplets, $N_{tot-mono} = 8 \cdot 10^6$, for the monodisperse population, is determined from the typical liquid water content $LWC_0 \sim 0.8 \text{g}/\text{m}^3$ encountered in warm cumulus clouds and the chosen initial monodisperse radius, $R_{0,mono} = 15 \mu\text{m}$,

$$N_{tot-mono} = LWC_0 \frac{4}{3} \pi \rho_w R_{0,mono}^3. \quad (7)$$

The faster dynamics of the droplet spectrum inside the highly intermittent mixing layer, with respect to that shown in the nearly Gaussian cloud turbulence, should be noted. Panels a and b in Fig. 2 highlight the intense acceleration of the broadening of the droplet spectrum in the interfacial layer (standard deviation time variation: $0.015(t/\tau_0) + 0.05$ in the cloud and $0.23(t/\tau_0) + 0.003$ in the mixing, see figures 7,11 and table 3 in Golshan et al. (2021)²³. Panels c and d in Fig. 2) show, for an initially flat polydisperse size distribution, a faster rate of modification toward the typical peaky shape in the interface than in the cloudy region. In fact, the temporal narrowing of the standard deviation goes like $-0.19(t/\tau_0) + 19.7$ in the cloud and as $-0.74(t/\tau_0) + 17.94$ in

the mixing, see figures 8,12 and table 3 in Golshan et al. (2021)²³.

Broad droplet size distributions have been observed in both in-situ measurements of forming shallow cumulus clouds¹⁵ and in laboratory experiments¹⁴. These distributions usually show a peak for relatively small radii ($1 \div 10\mu\text{m}$), which is accompanied by a monotonical decrease in concentration as the radius increases. However, the existence of a general and ubiquitous functional shape of the droplet size distribution in shallow cumulus clouds is still a matter of debate³⁵. Without any claim of generality, we introduce an initial polydisperse distribution in which the same mass is allocated to each class of radii. Each volume class gathers droplets that have roughly the same volume²³.

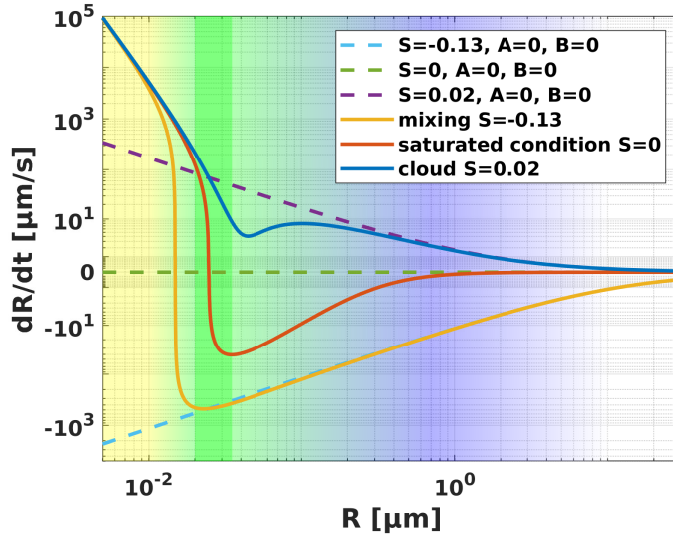


FIG. 3: The plot shows the condensational growth rate (Equation 8) for a drop of given radius R for supersaturated ($S = 0.02$, as in the cloud region of the present work), saturated ($S = 0$) and subsaturated ($S = -0.3$) conditions. The contributions due to the effect of both surface tension (Kelvin) and curvature (Raoult) are negligible for droplets of radius above $1\mu\text{m}$, such as the ones considered in the present work. The dashed lines only represent the effect of supersaturation, when the Kelvin and Raoult terms are set equal to zero. The vertical green bar highlights the range of radii below-above which the Raoult and Kelvin terms dominate, respectively.

A droplet is subject to ambient supersaturation, which is obtained through a polynomial interpolation with the neighboring cell values. The condensation-evaporation rate of the spherical j -th droplet can be estimated according to^{6,12,36}

$$\frac{dR_k}{dt} = \frac{K_s}{R_k} \left(S - \frac{A}{R_k} + \frac{Br_d^3}{R_k^3} \right) \quad (8)$$

where S is the supersaturation or saturation deficit (see section IID), A is the Kelvin coefficient, B is the hygroscopicity parameter, R_k is the k -th droplet radius, and r_d is the accumulation radius. The second and the third terms on the right-hand side are known as the Kelvin and Raoult terms,

respectively. The Kelvin term describes the effect of droplet curvature and surface tension, while the Raoult term indicates aerosol hygroscopicity. The diffusion coefficient K_s is slightly sensitive to local equilibrium thermodynamics^{7,36,37}. It includes the self-limiting effects of latent heat release. This diffusion coefficient is considered to be constant in the literature, for typical warm cloud conditions, where the characteristic heat flux due to latent heat from a small variation in the droplet temperature is of the same order as the heat flux due to thermal conduction for the same temperature difference. The temperature dependence of this constant is weak (the K_s value in $\text{m}^2 \text{s}^{-1}$ ranges from $5.07 \cdot 10^{-11}$ at $T = 270 \text{ K}$, to $1.17 \cdot 10^{-10}$ at $T = 293 \text{ K}$ ^{17,38}). In agreement with our volume averaged initial temperature of 281 K, we used the value $8.6 \cdot 10^{-11} \text{ m}^2 \text{ s}^{-1}$. The interpolation of Eulerian field values at grid points to the position occupied by the water droplets inside the cell is obtained via second-order Lagrange polynomials. An inverse procedure is then used for the calculate of the condensation rate, which is determined at the first step at each droplet position and then relocated to the closest of the eight grid vertices. A collision is hypothesized to occur when the distance between the centers is equal to or less than the sum of their radii. Such collisions are assumed to be completely inelastic.

Supersaturation

$$S(\mathbf{x}, t) = \frac{\rho_v(\mathbf{x}, t)}{\rho_{vs}(T)} - 1 = RH - 1$$

is defined as the ratio between the water vapor and the saturated vapor densities (i.e. the relative humidity) minus 1. The relative humidity $RH = \rho_v/\rho_{sv}$ and supersaturation (or saturation deficit) are functions of the saturated vapor density, ρ_{vs} , whose dependence on temperature is described by the Clausius-Clapeyron equation⁷

$$\frac{d\rho_{vs}}{\rho_{vs}} = \left(\frac{\mathcal{L}}{R_v T} - 1 \right) \frac{dT}{T} \quad (9)$$

where \mathcal{L} is the latent heat of evaporation (condensation) and R_v is the gas constant of the water vapor. It is hypothesized that the droplet-gas interphase coupling is negligible³⁹, and the droplet motion therefore does not exert any relevant dynamical effect on the carrier field. Conversely, the turbulent field affects the motion of the water drops to a great extent. Phase transition at the droplet surface results in the exchange of water vapor and latent heat between the two phases, thus perturbing the buoyancy term in momentum equation (2b).

Since the coefficients A , B , and r_d are hypothesized to be constant, the droplet growth rate mainly depends on the local value of S and on the droplet radius R . The droplet growth (shrinkage) rate (8) is plotted in Figure 3 for three constant values of supersaturation S , where the competing effects of the Kelvin and Raoult terms can be appreciated by observing the orange curve, which describes a saturated environment. In the present conditions, the Kelvin effect becomes important for $R < 1 \mu\text{m}$, and it is soon outweighed by the Raoult effect as the droplet (aerosol) radius falls below $\cong 23 \text{ nm}$. The Raoult term is the term that is prevalent below this threshold.

C. Numerical experiment. Computational domain, initial and boundary conditions and DNS algorithm

All the numerical experiments discussed in this paper have been performed over a 3D $512^2 \times 1024$ cartesian mesh grid²³. This parallelepiped-shaped domain (see Figure 1) is made up of two adjacent cubes of 512^3 cells each. The volume of the domain is L_{12}^3 , with L_{12} being the length of each cube edge. Two initial zero-mean, homogeneous, isotropic air fluctuation fields are generated inside the two cubes. The turbulent spectra show the same functional shape and hence the same integral scale. The cube in the lower half of the parallelepiped - which from now on is referred to as the cloud region - initially hosts a higher turbulent kinetic energy, E , and dissipation (*decay*) rate, ε , than the upper cube, which models a clear air region, see Figures 1b and 4, Panels a and b. The initial integral scale is set equal in the two regions so as not to introduce a further control parameter - the integral length gradient across the layer - on the interface evolution and the related transport dynamics^{25,27}.

The root mean square velocity in the more energetic region is $u_{rms} \cong 0.11 \text{ m s}^{-1}$, which represents the large-scale energy in the cumulus spectral subrange of wavelengths 0.002 to 0.25 m. Since our system is time decaying, the initial dissipation rate was purposely set high in order to reach the commonly values observed in cumulus clouds in the central part of the transient. However, the initial dissipation rate $\varepsilon \sim 500 \text{ cm}^2/\text{s}^3$ is of the same order as those measured by⁴⁰ in cumulus clouds in the proximity of the top (cloud # 1 measurement, 100 m below the cloud top, height of the top 4800 m) although in the presence of a much higher kinetic energy of the air fluctuation ($rms \sim 2 \text{ m/s}$). Lower values ($10 \sim 20 \text{ cm}^2/\text{s}^3$) have been reported by⁴¹⁻⁴⁴, and they are obtained during the transient decay, see Fig.s 4, Panels c and d. The estimated Kolmogorov scale is $\eta_1 \sim (v^3/\varepsilon_1)^{1/4} \cong 0.5 \text{ mm}$. The edge of a cube grid cell in the physical domain is $\Delta x = 1 \text{ mm}$, and the highest resolved wavenumber is $k_{max} = \pi/\Delta x = \pi \cdot 10^3 \text{ m}^{-1}$ ⁴⁵. Since we have $k_{max}\eta_1 \cong 1.6$, the resolution is acceptable for the problem at hand^{33,46}. An appropriate time step for advancement is computed from the initial u_{rms} values of the more energetic cloudy region $\Delta t = 4.7 \cdot 10^{-4} \text{ s}$.

D. Initial and boundary conditions for the flow velocity, temperature and vapor fields

Two homogeneous isotropic solenoidal turbulent fields, with zero-mean velocity and different kinetic energies, that mix at a common interface, are studied in this numerical experiment. A smoothing function, $p(x_3)$, is applied to modulate the velocity and scalar vapor fields along x_3 ^{27,28}

$$u_i(x_j) = u_{i1}(x_j)p(x_3) + u_{i2}(x_j)\sqrt{1 - p^2(x_3)}$$

$$\rho_v = \rho_{v1}p(x_3) + \rho_{v2}\sqrt{1 - p^2(x_3)}$$

$$p(x_3) = 1 + \tanh\left[a\frac{x_3}{L_3}\right] \tanh\left[a\left(\frac{x_3}{L_3} - \frac{1}{2}\right)\right] \tanh\left[a\left(\frac{x_3}{L_3} - 1\right)\right]$$

where $\rho_{v1} = \rho_{vs}(T_1)RH_1$ and $\rho_{v2} = \rho_{vs}(T_2)RH_2$ were chosen to obtain the desired level of supersaturation in both regions (see Table I). Direction x_3 is the inhomogeneous direction and L_3 is the width of the computational domain in the x_3 direction. Constant a determines the initial mixing layer thickness Δ , which is conventionally defined as the distance between the points with normalized energy values of 0.25 and 0.75, whenever the low energy side is mapped to zero and the high energy side to one. When $a = 12\pi$, the initial Δ/L_3 ratio is about 0.026, a value that was chosen so that the initial thickness would be large enough to be resolved but small enough to have large regions of homogeneous turbulence during the simulations.

The initial distributions of the velocity, temperature and water vapor density fields in the vertical direction are plotted in Figure 1 a.

The same initial values of T and ρ_v are defined for all the cells of a horizontal plane and are thus functions of their vertical position with respect to the interface. As in^{23,47}, the vapor field is periodic and continuous in the three directions, whereas the temperature field

$$T(x_3, 0) = T'(x_3, 0) + T_0 + G\frac{x_3}{L_3} \quad (10)$$

is composed of the sum of a vertical, triple-periodic fluctuating temperature $T'(x_3, t)$, a static component Gx_3 , and a global average temperature T_0 . The periodic term T' in equation (10) is defined with a hyperbolic tangent

$$T'(x_3, 0) = \frac{T_2 - T_1}{2} \cdot \left[\tanh\left(a\left(\frac{x_3}{L_3} - \frac{1}{2}\right)\right) - \frac{2x_3}{L_3} + 1 \right] \quad (11)$$

However, the code is required to solve the periodic field T' . Equation (2c) then becomes

$$\frac{\partial T'}{\partial t} + u_1 \frac{\partial T'}{\partial x_1} + u_2 \frac{\partial T'}{\partial x_2} + u_3 \frac{\partial (T' + Gx_3)}{\partial x_3} = \kappa \nabla^2 T' + \frac{\mathcal{L}C_d}{\rho_0 c_p}$$

The cloud-clear air interface is located in the center $(x_3 - x_c)/L_3 \cong 0$, with $x_c = L_{12}$. We define the distance between the points whose normalized temperature $(T - T_{min})/(T_{max} - T_{min})$ is 0.75 and 0.25, respectively, as the width of mixing layer region Δ ^{24,27,48}. The squared Brunt-Väisälä frequency, $\mathcal{N}^2 = g \frac{\delta T}{T_0} \frac{1}{\Delta} \cong -0.69 \text{ Hz}^2$, is negative, and thus describes an unstable environment. The internal Froude number associated with this stratification is initially

$$\text{Fr}_{int}^2 = \frac{u_{rms,av}^2}{\mathcal{N}^2 \Delta^2} \cong -7$$

The saturated vapor density, the relative humidity and the supersaturation are computed with the values of T expressed by equation (10).

E. DNS algorithm

The DNS algorithm is based on the dealiased pseudospectral Navier-Stokes solver described in⁴⁹. Code versions and releases are available on the official Philofluid Research Group website.

TABLE I: The key physical parameters used in the numerical experiments.

Quantity	Symbol	Value	Unit
Latent heat of evaporation	\mathcal{L}	$2.48 \cdot 10^6$	Jkg^{-1}
Heat capacity of the air at a constant pressure	c_p	1005	$\text{Jkg}^{-1} \text{K}^{-1}$
Gravitational acceleration	g	9.81	m/s^2
Molar mass of the water	\mathcal{M}_w	18	kg kmol^{-1}
Gas constant of the water vapor	R_v	461.5	$\text{Jkg}^{-1} \text{K}^{-1}$
Molar mass of the dry air	\mathcal{M}_a	29	kg kmol^{-1}
Gas constant of the air	R_a	286.7	$\text{Jkg}^{-1} \text{K}^{-1}$
Diffusivity of the water vapor mass	κ_v	$2.52 \cdot 10^{-5}$	m^2/s
Thermal conductivity of the dry air	K	$2.5 \cdot 10^{-2}$	$\text{W m}^{-1} \text{K}^{-1}$
Liquid water density	ρ_w	1000	kg/m^3
Dry air density at an altitude of 1000 m	ρ_0	1.11	kg/m^3
Dry air kinematic viscosity	ν	$1.5 \cdot 10^{-5}$	m^2/s
Average temperature of the whole domain	T_0	281.16	K
Average temperature of the cloud region	T_1	282.16	K
Average temperature of the clear air region	T_2	280.16	K
Background temperature gradient (unstable)	G	-2/1.024	K m^{-1}
Brunt-Väisälä amplification factor	\mathcal{N}^2	-0.69	s^{-2}
Droplet growth coefficient	K_s	$8.6 \cdot 10^{-11}$	m^2/s
Accumulation mode (radius)	r_d	0.01	μm
Kelvin coefficient	A	$1.15 \cdot 10^{-9}$	m
Raoult solubility parameter for inorganic, hygroscopic substances such as ammonium sulfate, lithium chloride etc...	B	0.7	-
Initial relative humidity in the cloud region	RH_1	1.02	-
Initial relative humidity in the clear air region	RH_2	0.7	-
Initial liquid water content	LWC_0	$7.9 \cdot 10^{-4}$	kg/m^3

This software has been used in several works conducted by the group^{23,24,26–28,47} to investigate turbulence self-diffusion in shearless mixings, with passive or active scalars, and water drop populations. Spectral discretization is achieved by means of the Fourier-Galerkin method with pseudo-spectral treatment of the advection terms in the momentum (2b) equation, and scalar transport ones (2d and 2c). Time integration is performed, according to Ireland (2012)³³, with a second-order explicit Runge-Kutta method⁵⁰. The diffusive terms for the momentum, internal energy (2c) and vapor density fields (2d) are computed by means of exponential integration. Droplet velocities 5a and accelerations 5b are integrated with a second-order explicit method and a second-order implicit trapezoidal method, respectively. The implicit structure of the integration scheme used for the equations 5b ensures numerical stability for arbitrary values of Δt .

TABLE II: The key simulation parameters and initial conditions, which are the same for all the runs.

Quantity	Symbol	Value	Unit
Domain size	$L_{1,2}^2 \cdot L_3$	$0.512^2 \cdot 1.024$	m^3
Domain discretization	$n_{1,2}^2 \cdot n_3$	$512^2 \cdot 1024$	-
Grid step	Δx	10^{-3}	m
Initial rms velocity (cloud)	$u_{rms,1}$	0.11	m s^{-1}
Initial integral scale	ℓ_0	$2.65 \cdot 10^{-2}$	m
Initial dissipation rate (cloud)	ε_1	0.05	m^2/s^3
Initial energy ratio (cloud-clear air)	$E_1/E_2 = u_{rms,1}^2/u_{rms,2}^2$	6.7	-
Initial Kolmogorov time (cloud)	$\tau_{\eta 0} = (\nu/\varepsilon_1)^{1/2}$	$1.74 \cdot 10^{-2}$	s
Initial Kolmogorov length scale (cloud)	$\eta_0 = (\nu^3/\varepsilon_1)^{1/4}$	$5.1 \cdot 10^{-4}$	m
Initial eddy turnover time	$\tau_0 = 2\ell/(u_{rms,1} + u_{rms,2})$	0.35	s
Initial Reynolds number (cloud)	$\text{Re}_\ell = u_{rms}\ell/\nu$	196	-
Droplet Response timescale ($1\mu\text{m}$, $30\mu\text{m}$)	$\tau_d = 2\rho_v R/9\rho_0\nu$	4.410^{-4} , 1.310^{-2}	s
Initial droplet Stokes numbers ($R \in 1 - 30 \mu\text{m}$)	$St = \tau_d/\tau_{\eta 0}$	0.025 - 0.7	
Final droplet Stokes number ($R \in 1 - 30 \mu\text{m}$)	$St = \tau_d/\tau_{\eta f}$	0.002 - 0.066	
Initial Taylor microscale Reynolds number	$\text{Re}_\lambda = u_{rms}\lambda/\nu$	52	-
Integration time step	$\Delta t = 1/20 \cdot \Delta x/u_{rms}$	$4.64 \cdot 10^{-4}$	s
Initial number of droplets (monodisperse distribution)	$N_{tot-mono}$	$8 \cdot 10^6$	-
Initial number of droplets (polydisperse distribution)	$N_{tot-poly}$	10^7	-
Initial droplet radius (monodisperse distribution)	$r_{0,mono}$	15	μm
Initial droplet radius (polydisperse distribution)	$r_{0,poly}$	$0.6 \div 30$	μm

The code stores the velocity, temperature and vapor fields in three-dimensional arrays and distributes them along one direction in both physical and Fourier spaces. The three-dimensional discrete Fourier transform is performed with the FFTW library. A slab-like parallelization is implemented with Message Passage Interface (MPI) standard libraries.

III. RESULTS. VELOCITY AND SUPERSATURATION FLUCTUATIONS, AND TURBULENCE BROADENING OF THE DROPLET SIZE DISTRIBUTION.

Droplet and flow statistics are taken from horizontal $x_1 - x_2$ planes at a constant x_3 , and plotted with respect to the normalized height $(x_3 - x_c)/L_3$, with x_c being the position of the cloud-clear air interface, and $L_3 = 2L_{1,2}$ being twice the length of the edge of the cube. To observe the interface cloud - clear air dynamics, it is necessary to focus on the evolution of the statistics along the non-homogeneous (vertical) direction of the domain. The mean, standard deviation and higher order-moments are computed over the cells in the same horizontal plane and associated with the

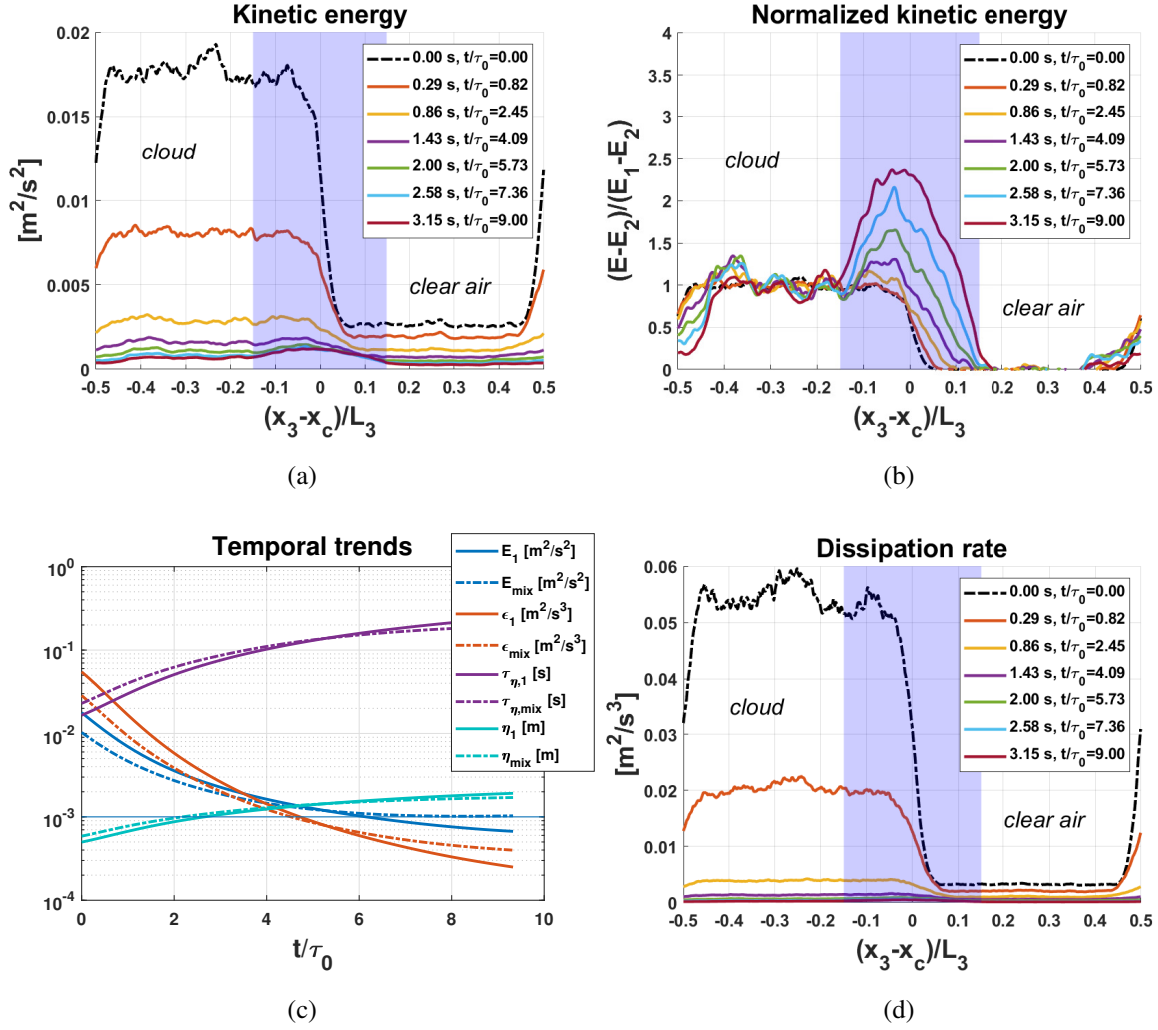


FIG. 4: **Trends of the kinetic energy and turbulent dissipation rate.** (a) Evolution of the turbulent kinetic energy E across the domain for an initial unstable background temperature gradient. The interface is located at the center of the figure (that is, for $x_3 \cong x_c$). Mildly unstable stratification ($\text{Fr}_{\text{int}}^2 \cong -7$). (b) Normalized values of $E(t)$ with respect to the mean kinetic energy in the cloud $E_1(t)$ and clear air $E_2(t)$ regions. The initial energy ratio across the interface is $E_1/E_2 = 6.7$. The plotted values of E are the planar averages of each horizontal plane. (c) Transient evolution of the kinetic energy E , the dissipation rate ϵ , the Kolmogorov time scale τ_η and the Kolmogorov length scale η in the cloud and mixing regions (subscripts 1 and 2, respectively). The thin horizontal line indicates the grid width, Δx , in meters. (d) Evolution of the dissipation rate ϵ across the domain.

corresponding vertical coordinate x_3 . The covariance for each horizontal plane

$$\text{cov}_{X,Y}(x_3, t) = \frac{1}{n_1 n_2} \sum_{i,j=1}^{n_1, n_2} (X(x_1, x_2; x_3, t) - \bar{X}) (Y(x_1, x_2; x_3, t) - \bar{Y}) \quad (12)$$

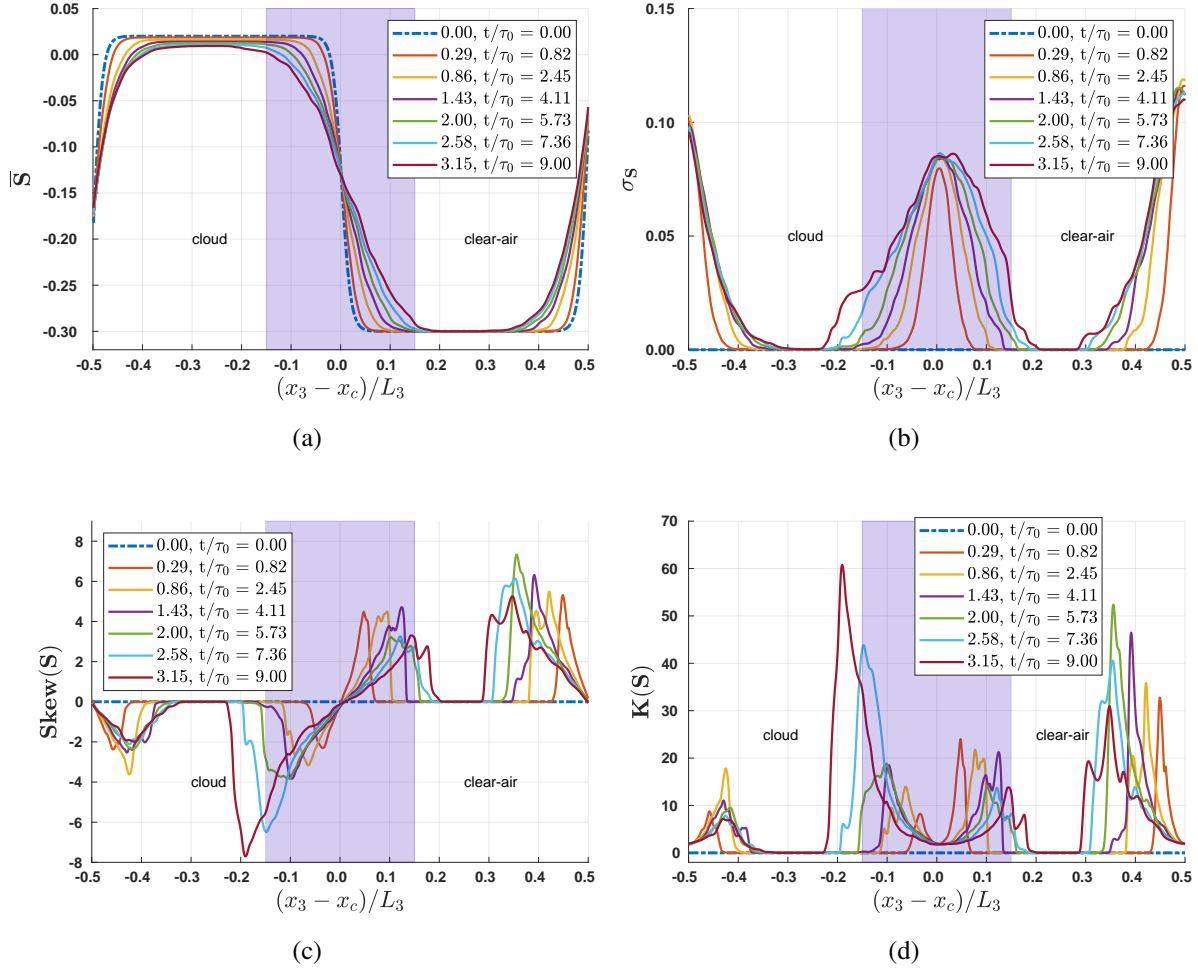


FIG. 5: Monodisperse droplet population. Planar averages and statistical moments of supersaturation across the cloudy - under-saturated ambient air interface layer. (a) Supersaturation (or saturation deficit) across the layer. (b) Standard deviation. (c) Skewness. (d) Kurtosis. The initial distributions are plotted with black dash-dotted lines. The approximate extension of the interface mixing layer is indicated as the blue-shaded area between the cloudy and clear air regions.

where the over-line indicates the average of a given physical quantity in the x_1, x_2 planes and

$$\bar{X}(x_3, t) = \frac{1}{n_1 n_2} \sum_{i=1, j=1}^{n_1, n_2} X(x_1, x_2; x_3, t) \quad (13)$$

The Pearson product-moment correlation coefficient of two planar averaged quantities, $\bar{X}(t)$ and $\bar{Y}(t)$, only depends on the time and when used to correlate variations across the interface layer $\Delta(t)$, it can be written as

$$\rho_{X, Y_{\Delta}(t)} = \sum_{k=1}^{n_{\Delta}} \frac{(\bar{X}(x_3, t) - \bar{X}_{\Delta}(t))}{\sigma_{\bar{X}}} \frac{(\bar{Y}(x_3, t) - \bar{Y}_{\Delta}(t))}{\sigma_{\bar{Y}}} \quad (14)$$

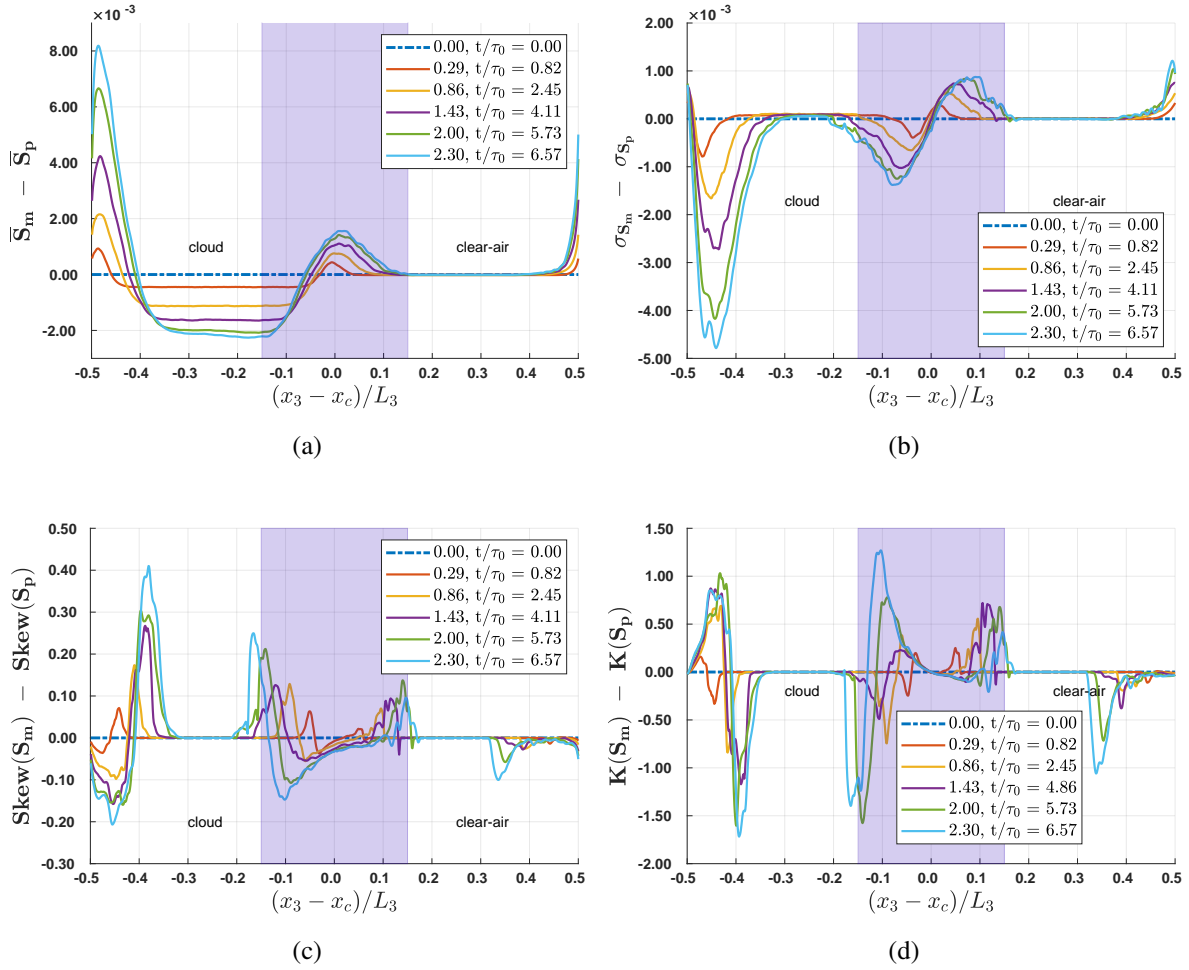


FIG. 6: Difference in the supersaturation statistics between monodisperse (S_m) and polydisperse (S_p) droplet populations across the cloudy - under-saturated ambient air interface layer. (a) Difference in the mean supersaturation (or saturation deficit) across the layer. (b) Difference in the standard deviation. (c) Difference in the skewness. (d) Difference in the kurtosis. The approximate extension of the interface mixing layer is indicated as the blue shaded area between the cloudy and clear air regions.

where subscript Δ stands for the quantity averaged inside the interface and n_Δ is the number of planes inside the interface.

The kinetic energy inside the homogeneous cloudy and clear air regions, decays over time with a power-law exponent (see Figure 4) of the $E/E_0 \sim (t/\tau_0)^{-n}$ type, where n ranges from 1.6 to 2.15^{27,51}. The initial values of the root mean square velocity of the flow, of the longitudinal integral length scale and of the eddy turnover time are reported in Table II. The eddy turnover time $\tau_0 = 2\ell_0/(u_{rms,c0} + u_{rms,a0})$, is computed from the initial integral length scale and root mean square velocity of the flow, averaged over the domain, and has an initial value of 0.35 s.

The decay of both kinetic energy E and dissipation rate ε can be observed in Figure 4). During

the decay, the integral scale grows homogeneously over the entire domain.

The system relaxes to a quasi steady-state condition as values of ε of the order of $10 \text{ cm}^2/\text{s}^3$ are reached inside the mixing layer. Values of this order of magnitude have already been measured in shallow cumulus clouds^{10,41}.

The average value of E quickly decreases during the transient. However, the effects of the unstable stratification are highlighted by the normalized kinetic energy, $(E - E_2)/E_1 - E_2$, which in fact shows a hump that amplifies in time (see Figure 4b, and Figures 11 and 12 in Gallana et al.²⁸). The warmer air close to the interface is convected upward and gains vertical velocity, thus increasing the kinetic energy locally. This injection of kinetic energy at the small scales of the turbulence affects the mixing process by enhancing the vertical advection of the dispersed water droplets, water vapor and internal energy up to the subsaturated region. High values of higher moments of the spatial longitudinal derivatives of the velocity indicate the high anisotropy and intermittency of the small-scale of the carrier flow in the mixing region. Small-scale intermittency in the mixing region is associated with accelerated droplet population dynamics and an increased collision-coalescence rate, see Figure 2 in section II and also Table 3 and Figures 11 and 12 in Golshan et al. 2021²³. The time required by the two populations to reach the same width for the evaporation and condensation processes is estimated by equating the time variations of the standard deviations of the monodisperse and polydisperse size distributions. The estimate is about $100\tau_0$ in the cloudy region, which is homogeneous and isotropic. The estimate is about $18,5\tau_0$ in the interface region, i.e. more than 5 times faster. A remarkable acceleration of the broadening of the droplet size distribution, due to turbulent fluctuations, is therefore observed in the shear-free mixing layer that separates the cloud from the sub-saturated environmental air.

Planar averages and higher order statistical moments of supersaturation across the cloudy - undersaturated ambient air interface layer are shown in Fig. 5. The high intermittency of the distributions should be noted. Very high values of both skewness and kurtosis are reached on the two sides of the mixing layer. Moreover, comparatively higher absolute values can be observed at the border with the cloudy region (S down to -8, K up to 60), where the vapor flux is spatially increasing, with respect to that observed at the border with sub-saturated air (S up to 4, K up to 20), where the vapor flux is spatially decreasing²⁸.

The droplet statistics have been computed over the horizontal planes to complement the data in Fig. 2. From now on, we denote the droplet numerical concentration with the symbol N . The results of the monodisperse and polydisperse distributions across the mixing layer are shown in Figure 7, where both the droplet radius and the concentration are plotted along x_3 . At the beginning of the transient, the droplets populate the lower part of the domain and are randomly distributed within the cloud. The core environment of the cloud is supersaturated (see Figure 5a), and this permits a uniform condensation growth of the droplets to take place within the cloud. As the central mixing proceeds, a few drops are advected in the upper subsaturated clear-air region. Here, smaller drops will rapidly evaporate and eventually be eliminated by the algorithm. Dissipation rate ε decreases during the transient and heavier droplets are likely to settle, as the small-scale Froude number scales sublinearly with the dissipation rate $\text{Fr}_\eta \sim \varepsilon^{3/410}$.

Mean droplet radius and concentration across the cloud and interfacial mixing regions

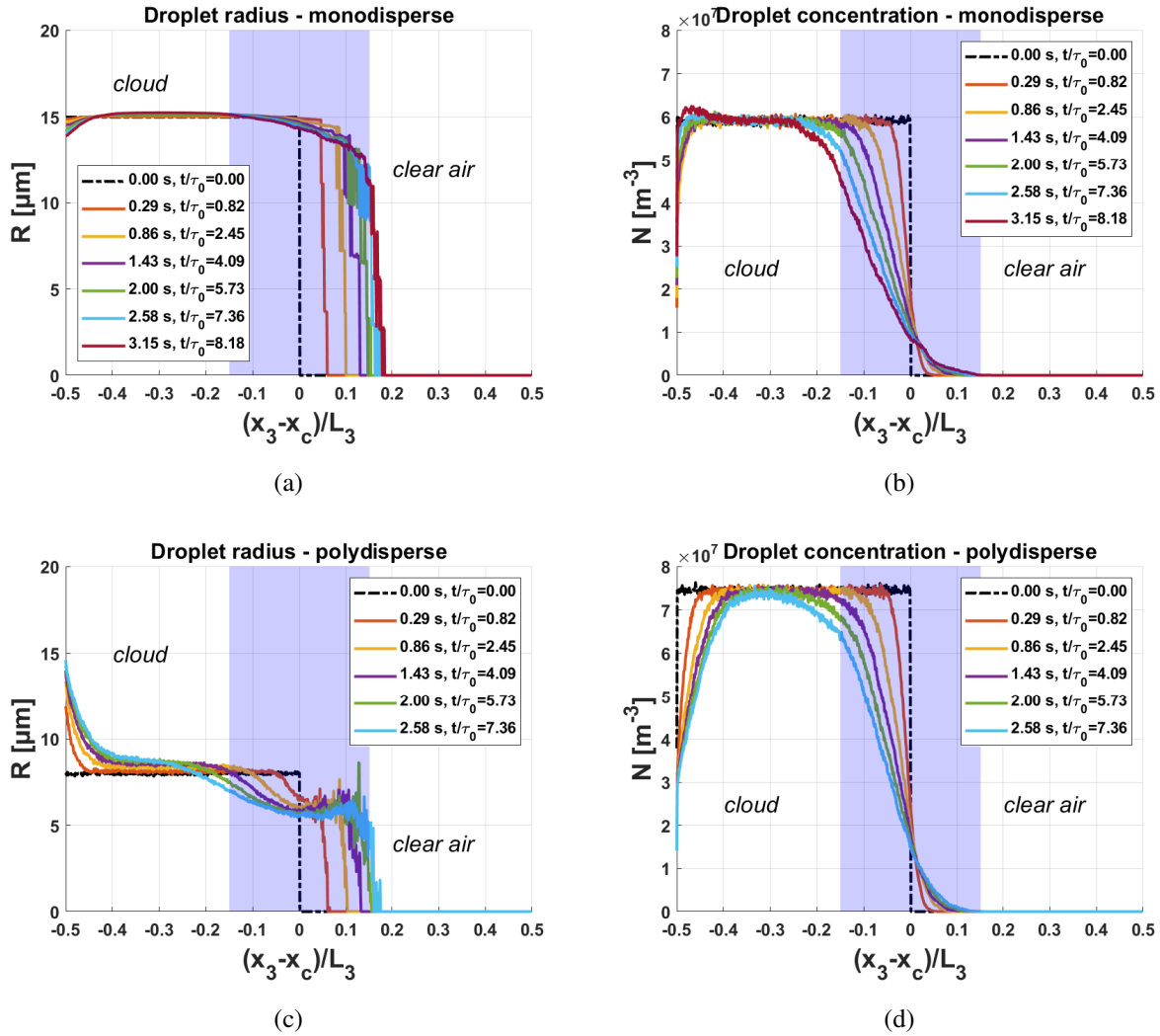


FIG. 7: Average mean droplet radius (a) (c), and concentration (b) (d). Each value represents the planar average computed for a horizontal plane (see Figure 1). Shearless mixing takes place in the shaded area. The dash-dotted black line shows the initial conditions.

The mean radius plot for the monodisperse case (see Figure 7a) is almost flat in the cloud core region. The extension of this constant-radius plateau becomes more and more reduced as the decaying shearless mixing proceeds. The blue-shaded area represents an approximate extension of the mixing region at the end of the simulated transients. The concentration plots (Figure 7b) displays analogous trends. In the polydisperse case, Figures 7c and 7d, the flat region of nearly constant radii is narrower and presents a peak close to the very top of the mixing layer. This is because collisions are much more frequent in this case. Moreover, given the concomitant presence of very different droplets, the volume ratio between the largest to the smallest droplet is of the

order of $1.25 \cdot 10^5$, thus the number of collisions is large. Out of a total of 10^7 droplets, we in fact observe about $5 \cdot 10^4$ collisions over about 8 physical time scales. Information on the collision kernel inside the cloudy and mixing layer regions can be found in Figures 13 and 14 of Golshan et al. 2021²³.

A. Supersaturation evolution equation, and the microphysical time scales.

The supersaturation evolution equation has often been used to model a water vapor budget on a developing cloud¹⁰. This equation is based on a production-condensation model, where the time derivative of supersaturation is determined by balancing a production term, \mathcal{P} , and a condensation term, \mathcal{C} ^{6,8}

$$\frac{dS}{dt} = \mathcal{P} + \mathcal{C} \quad (15)$$

The condensation term accounts for the depletion of water vapor and the release of latent heat during condensation at the surface of a spherical droplet, and it is a function of the local level of supersaturation

$$\mathcal{C} = -\frac{S}{\tau_{phase}} = 4\pi\kappa_v N \bar{R} S. \quad (16)$$

The source term, \mathcal{P} , has often been modeled as a linear function of the vertical mean velocity of the updraft^{12,15}, or identified as the net flux of supersaturated water vapor through the parcel boundaries¹⁶. In the present analysis, updraft is absent, thus $\mathcal{P} = 0$. Equation (15) does not account for the advection and diffusion of water vapor and internal energy in the environment surrounding the droplet ($Re_{drop} \ll 1$), and considers supersaturation S as a rather global, bulk property of an adiabatic cloud parcel⁷. In their study on cloud cores,¹³ generalized the supersaturation evolution equation (15) to a transport model by assuming a linear dependency between the diffusive term of the supersaturation and the Laplacian of the temperature and vapor density fields. They showed that, under steady-state conditions and within the limit of a real-cloud Reynolds' number, the diffusive term of the supersaturation variance becomes negligible.

In a homogeneous, nearly isotropic cloudy layer that is statistically in equilibrium, a zero-mean vertical velocity field would imply a null net vertical transport of cooling vapor parcels. It should be noted that whenever an updraft can be neglected, equation (15) can be solved by separating the variables⁵²

$$\frac{dS}{dt} \cong -4\pi\kappa_v N \bar{R} S = -\frac{S}{\tau_{phase}} \quad (17)$$

Therefore, an initially subsaturated (supersaturated), droplet-laden environment experiences an increase (decrease) in the vapor concentration, which results in S relaxing exponentially to 0. The time constant of this solution is the phase relaxation time

$$\tau_{phase} = (4\pi\kappa_v N \bar{R})^{-1} \quad (18)$$

Microphysical time scales and mean supersaturation in the cloud and interfacial mixing regions

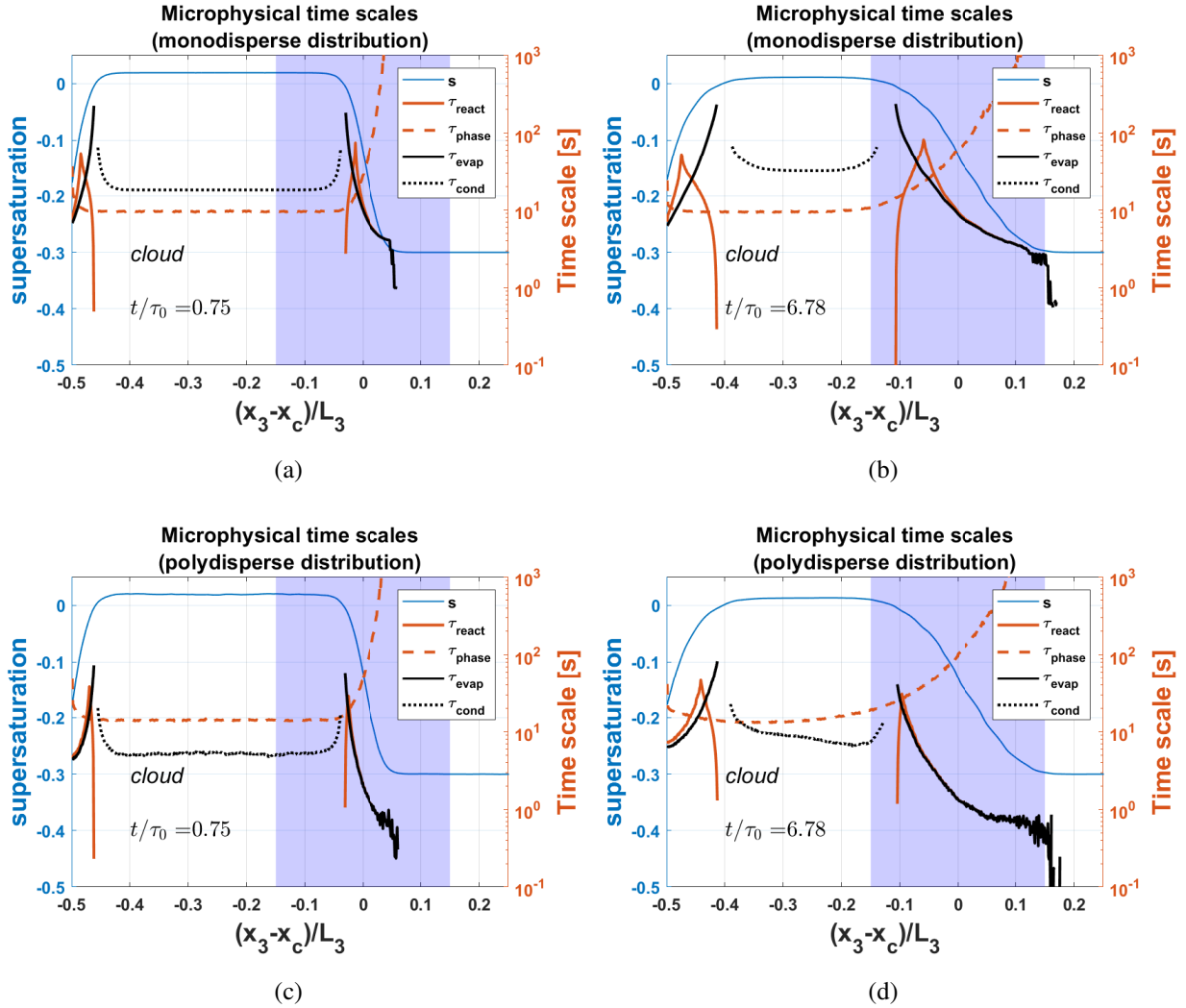


FIG. 8: Vertical distribution of the evaporation τ_{evap} , phase relaxation τ_{phase} and reaction τ_{react} time scales computed inside each grid cell and then averaged on horizontal planes. The data are displayed for the monodisperse (a) (b), and the polydisperse cases (c) (d) for two different time steps at the beginning and the end of the transient. The planar average of supersaturation \bar{s} (Figure 5a) is also plotted for comparison purposes.

The definition of τ_{phase} depends on the assumption of the droplet population having a constant integral radius, $N\bar{R}$, and it is able to describe the temporal variation of the supersaturation and the liquid water content^{5,43} in a homogeneous context. The phase relaxation time was chosen from the microphysical time scales used in several DNS studies that focused on entrainment-mixing

processes^{4,14,17,19,31}, and was used to define the Damköhler number

$$Da = \frac{\tau_{turb}}{\tau_{microphysics}}$$

Depending on whether the choice of τ_{turb} falls into large or small-eddy time scales, a vast range of Damköhler numbers can be defined for the same microphysical time scale in a turbulent flow⁴. Large and small values of Da are associated with a fast and slow microphysical response of the droplet population to entrainment and turbulent mixing, respectively⁵³. Large Da are also associated with inhomogeneous mixing, whereas small Da often indicate homogeneous mixing^{2,3}.

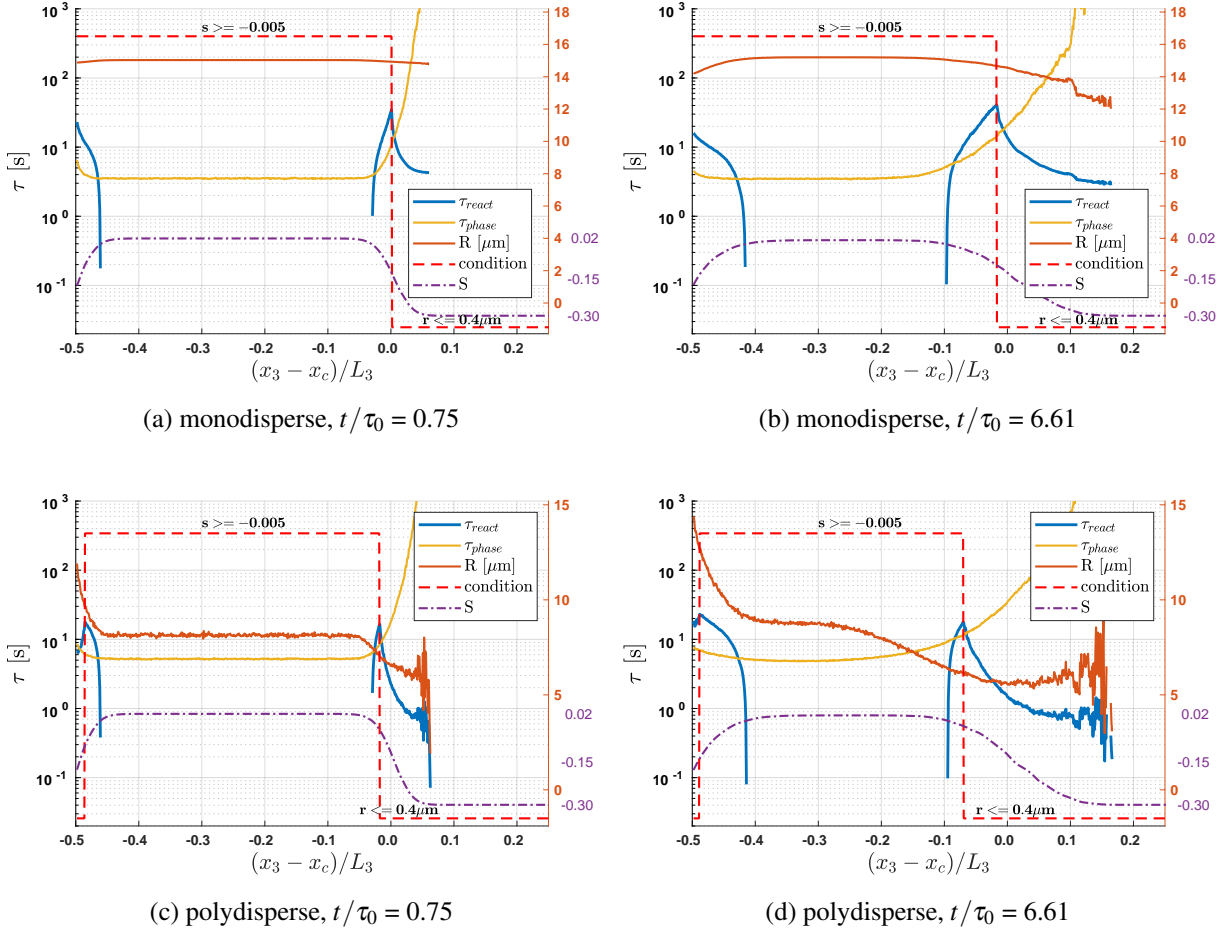


FIG. 9: For comparison with Fig. 8, the reaction time and relaxation phase time statistics, computed using planar averaged quantities, are here shown for both polydisperse and monodisperse populations and for two different time instances. The red dashed line represents the condition that is first reached at each vertical location when numerically solving the coupled system of Equations 8 and 17. Supersaturation S and the planar averaged R are included for reading convenience purposes.

However, it should be noted that, in a highly anisotropic, in-homogeneous situation, such as inside the mixing layer that separates the cloud from the subsaturated environmental air, the

momentum, internal and kinetic energy fluxes and the water vapor are not zero. The fluxes are positive and rising, forming a peak value that is almost centered in the middle of the layer. Beyond this point, the fluxes decrease and become zero inside the isotropic homogeneous subsaturated ambient air,^{48,26,28}. In such a situation, a mismatch between the supersaturation time derivative and the condensation term can be expected.

On the other hand, if the focus is on the evolution of the droplet size and the number concentration, the evaporation time scale offers a good practical description of the process, and should be taken as the relevant microphysical time scale, $\tau_{microphysics}$. By neglecting the Kelvin and Raoult terms in equation (8), and integrating for a constant $S_0 < 0$, one can obtain in each computational cell, an estimate of the time required for a single droplet, with an initial radius of R_0 , to evaporate completely in a uniform subsaturated environment

$$\tau_{evap} = -\frac{R_0^2}{2K_s S_0} \quad (19)$$

Both τ_{phase} and τ_{evap} rely on the assumption of constant supersaturation and integral radius. However, since both quantities vary concurrently inside a mixing layer, it is better to define a reaction time τ_{react} ⁴³ that considers variations of both S and $N\bar{R}$. The reaction time is defined as the shortest time that has elapsed since either the droplet has evaporated completely or the parcel has become saturated, and it is obtained by numerically solving the coupled system of differential equations, that is, Equations (8) and (17), for initial non-zero values of positive R_0 and negative S_0 . It should be noted that τ_{evap} and τ_{react} are only defined for the subsaturated regions, whereas τ_{phase} is defined for non-zero values of the integral radius, and can also be used in supersaturated regions. In order to describe a characteristic time of the condensation process in supersaturated regions of the domain, we introduce a condensation time τ_{cond} , which we arbitrarily define as the time it takes a droplet to double its radius for a constant local supersaturation S :

$$\tau_{cond} = \frac{3}{2} \frac{R_0^2}{K_s S_0}. \quad (20)$$

The horizontal planar average values of all these microphysical time scales are plotted for two different time instants and the initial droplet size distribution type in the cloud and mixing regions. See Figure 8, where the computation is performed in each computational grid cell and then averaged over the horizontal planes. For comparison, see also Figure 9, where the computation is performed by directly using the averaged quantities, \bar{R} and \bar{S} . It should be noted that the differently computed quantities are very close, except for the case of the monodisperse population at $t/\tau = 6.78$, where the location of the maximum reaction time changes from $(x_3 - x_c)/L_3 = -0.06$, Fig. 8, to $(x_3 - x_c)/L_3 = -0.025$, Fig. 9.

The condensation and evaporation times diverge toward values of the order of 10^3 seconds at the saturation location, $S = 0$, where they are not defined, see Figure 5a to observe the displacement in time of the spatial points where $S = 0$. The phase relaxation time, τ_{phase} , elongates across the mixing layer as the mean radius and the droplet concentration (numerical density) decrease. In

time, the τ_{phase} growth rate smoothes out as the layer widens. The fact that τ_{phase} grows indefinitely in the diluted interfacial region is not surprising and was also observed during the in-situ measurements of shallow cumulus clouds by Siebert and Shaw (2017)¹⁵.

It is interesting to observe that, in the monodisperse case, the reaction time is converging to the saturation time (ratio $\rho_v/\rho_{vs} = 0.995$), where the skewness of S is negative, while it is converging to the evaporation time when S is positively skewed.

The droplet condensation time is considerably higher everywhere than the phase relaxation time in the monodisperse case, and increases in time. The condensation time is instead shorter than the phase relaxation time in the cloudy region in the polydisperse case, but it becomes of the same order as τ_{phase} where the mixing process starts. A rise of τ_{cond} is observed at the end of the transient in the bottom region of the domain where the sedimentation due to gravity becomes substantial.

However, the most interesting observation is that there is a location inside the mixing layer where the phase relaxation, the reaction time and the evaporation time cluster together. This location precedes the location where the turbulent fluxes maximize. By comparing the distributions in Figure 8 with the distribution of the turbulent supersaturation flux, see Figure 10, it is possible to see that the clustering of the microphysical times takes place at almost the same location, where the flux rate is close to a maximum. The microphysical times separate before and after this location. In particular, the reaction time is much shorter than the evaporation and phase relaxation times before this location. The reaction time then collapses to the evaporation time, which is much shorter than the phase relaxation time. In the polydisperse case, the clustering of the microphysical times also includes the condensation time, as expected, since condensation often occurs rapidly in the spectral range of the drops with a small radius for these populations. The evaporation time on the right hand side of the panels in Figure 8 oscillates to great extent, particularly for the two panels showing the last part of the transient, due to the higher collision rate there. This result should be contrasted with Figure 2.

B. Turbulent transport effects on the supersaturation balance

The observed acceleration of the population dynamics in the same cloud-clear air interface region as those studied here, as well as the rapid differentiation in the size of the droplets, due to the different weights that evaporation, condensation and collision have in these highly intermittent mixing region²³, can, at least in part, explain the rapid increase in the size of the droplets that is observed in some cumulus cloud formations, in particular in maritime ones, and which is considered capable of locally inducing rain-fall, Mason and Chien (1962)⁵⁴, Li et al. (2020)⁵⁵. These findings have been observed despite the fact that beyond the temporal decay of the turbulence present in the whole system, the interface also hosts the spatial decay of the kinetic energy. It should be considered that the large scales of turbulence vary very little in this flow system, because the computational domain is fixed and because the ratio of the large scales and the ratio of the ki-

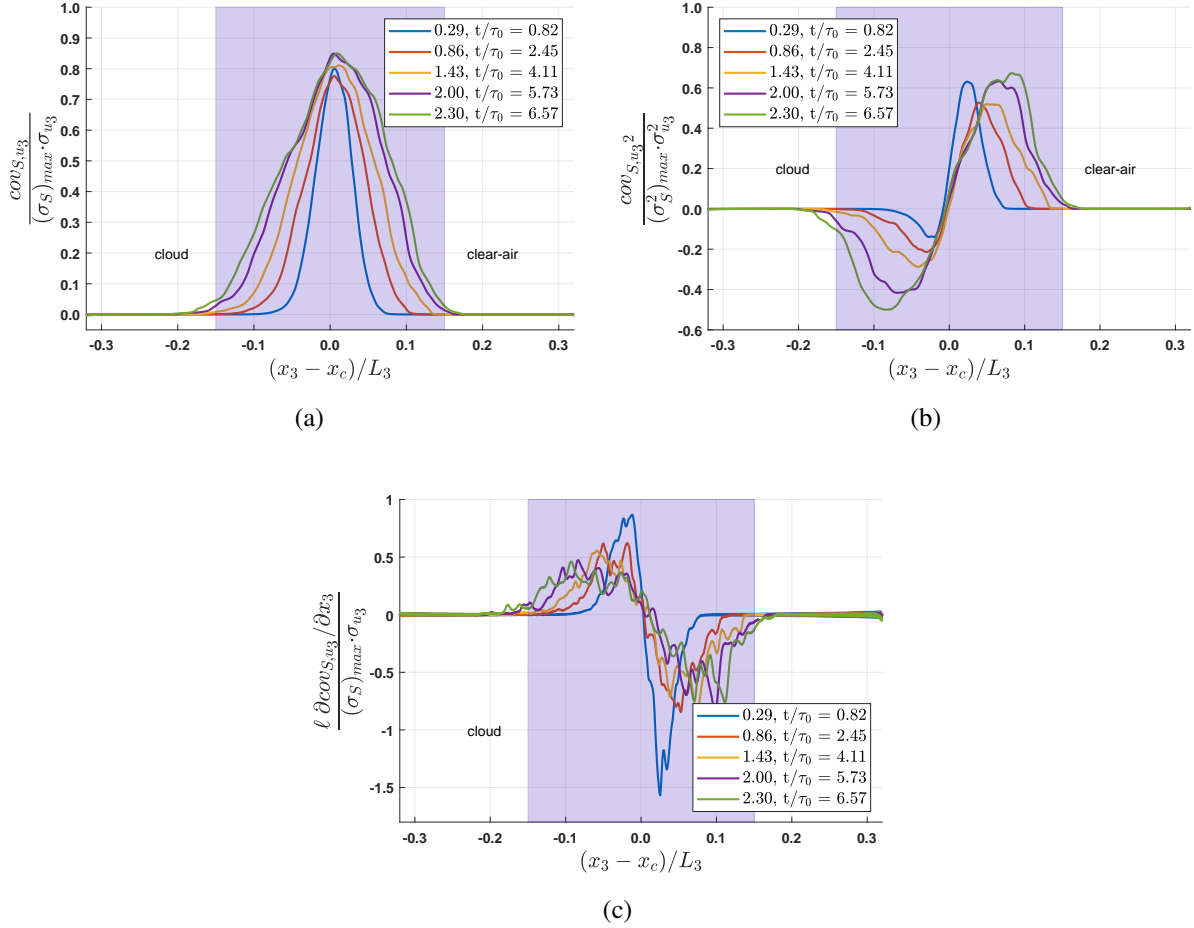


FIG. 10: Supersaturation flux statistics for the monodisperse drop population. (a) Normalized covariance (flux) of the supersaturation with vertical velocity component. (b) Normalized covariance of the supersaturation and square of the vertical velocity component. (c) Normalized derivative of the covariance (flux) of the supersaturation with vertical velocity component. The difference of values between the monodisperse and polydisperse population distributions is negligible. The same comparative situation shown in Figures 5 and 6 holds true.

netic energies between the cloudy and ambient air regions vary slowly in time^{24,27}. All things considered, these observations lead to the conclusion that the observed accelerated dynamics is associated with the particular small-scale anisotropy and intermittency of the interfacial layer.

In conditions of zero updraft, under almost statistical equilibrium conditions (steady state, homogeneity and isotropy), the planar averages of the difference between the time derivative of the supersaturation and the condensation terms must be null

$$\overline{dS/dt} - \overline{\mathcal{C}} = \overline{dS/dt} + \overline{S/\tau_p} \cong 0.$$

However, in more general turbulence situations, as in the present system, which is unsteady (a temporal decay follows an initial transient kinetic energy growth due to an unstable stratification),

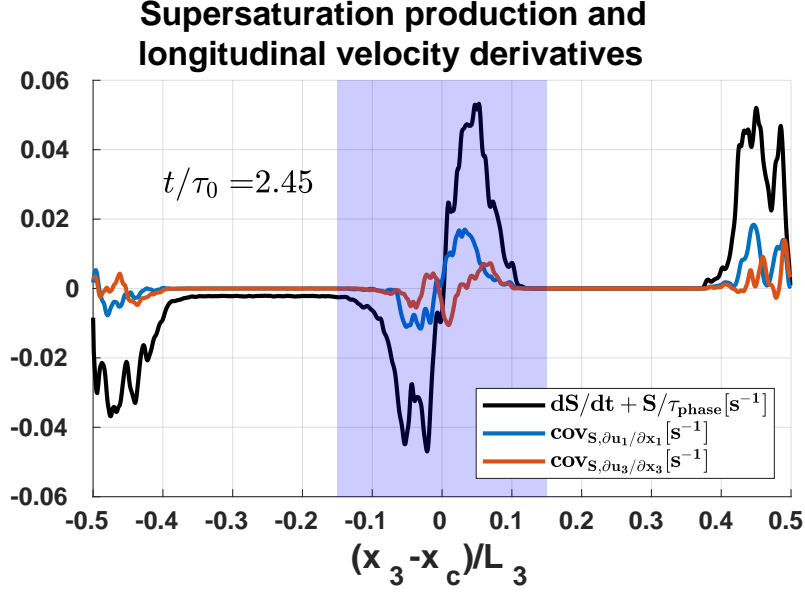


FIG. 11: Distribution of the planar horizontal averages along the vertical direction of the difference between the time derivatives of the supersaturation and condensation terms, $\overline{dS/dt} - \overline{C} = \overline{dS/dt} + \overline{S/\tau_p}$ and of the covariances $\text{cov}_{S, \partial u_1 / \partial x_1}$, $\text{cov}_{S, \partial u_3 / \partial x_3}$, see equation (12). These quantities vary considerably inside the mixing layer, and the two kinds of curves are both almost antisymmetric with respect to the center of mixing layer x_c . The data were retrieved from a monodisperse simulation at $t/\tau_0 = 2.45$.

highly in-homogenous, and thus anisotropic, $\overline{dS/dt}$ may not necessarily balance $\overline{S/\tau_p}$. This imbalance can be referred to as a turbulence supersaturation fluctuation production, $\overline{\mathcal{P}_t}$. As can be seen in Fig. 11, $\overline{dS/dt} + \overline{S/\tau_p}$ and the covariances between the supersaturation and the longitudinal velocity derivatives along the vertical direction, $\text{cov}_{S, \partial u_3 / \partial x_3}$, as well as along the horizontal direction $\text{cov}_{S, \partial u_1 / \partial x_1}$, are plotted across the entire $(x_3 - x_c)/L_3 \in [-0.5, 0.5]$ domain. All the quantities become larger and almost antisymmetric in the mixing region, and they appear qualitatively skew-symmetric with respect to the central plane $x_3 \cong x_c$. It is thus evident that, under spatially averaged (planar averages) conditions, the condensation term alone in the supersaturation evolution equation (15) is not able to account for the value of the time derivative of the supersaturation that takes place inside the mixing region.

Provided that the Kolmogorov time, τ_η , scales with dissipation rate ε , the former is found to be much smaller ($10^{-2} \div 10^{-1}$ s) than the evaporation and phase relaxation time scales reported in Fig. 8. Large values of τ_{phase} at the interface result in low small-scale Damköhler numbers, and should therefore enhance turbulent supersaturation fluctuations¹⁵. It is therefore reasonable to assume that supersaturation fluctuations, due to turbulence, are prevalent with respect to those generated by phase transition at the droplet surface. There are two reasons for this hypothesis. First, the statistical moments of the vapor density in an analogous unstable mixing layer with identical initial and boundary conditions and an identical set of control parameters for the carrier flow, but with

Supersaturation and longitudinal velocity derivatives in the mixing layer

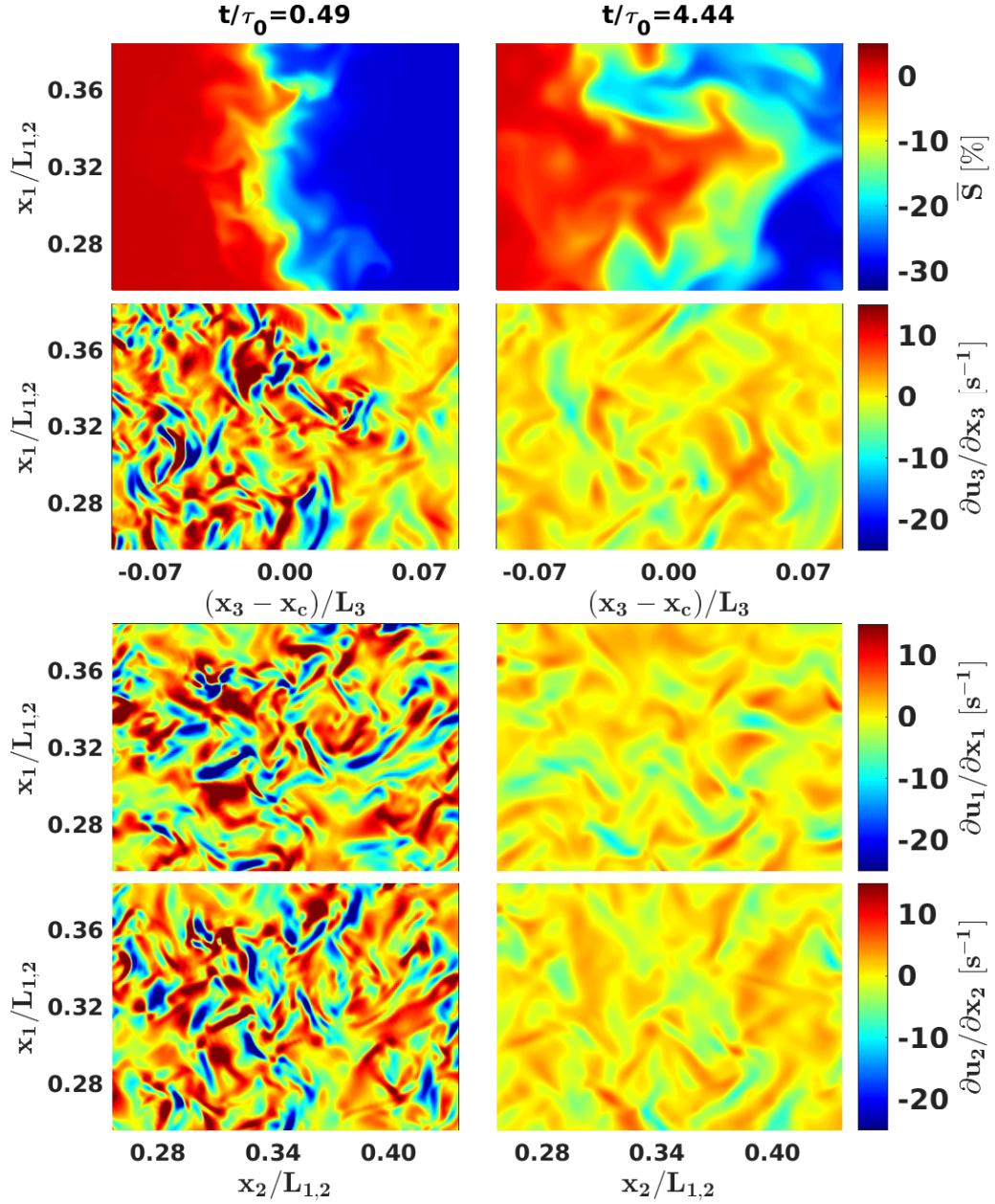


FIG. 12: Visualizations of the supersaturation (top row) and longitudinal velocity derivatives in the mixing region (second, third and fourth rows). The plots display only a portion of the domain, as shown by the normalized coordinates at two time instances $t/\tau_0 = 0.49$ (a) and $t/\tau_0 = 4.44$ (b). x_c denotes the initial position of the mixing layer. The variance of the longitudinal velocity derivatives is of the order of 10s^{-1} at the beginning of the transient, but rapidly decreases. The values of the inverse Kolmogorov times in the mixing region are plotted in Figure 4c (indigo dash-dotted line) and are of the same order of magnitude as the derivatives shown in this figure.

a subsaturated cloud region where droplets are absent, are close in shape and value to those of

mixings that contain droplets coming from a supersaturated cloudy region (see Figure 8 in²⁸) Second, as can be seen in Figures 5 and 6, the effects of the supersaturation statistics associated with the different size distributions of the drop populations are negligible, and the differences are in fact well below 1%. It should be noted that the opposite is not true, that is, that the dynamics of the populations is very sensitive to the shape of the droplet size distribution.

We therefore hypothesize that the amplitude of the local supersaturation is modulated by small-scale turbulent fluctuations and that such turbulent fluctuations may contribute to the overall local supersaturation balance. In order to assess this hypothesis, we looked for the proportionality relation between: i) the difference in the planar averages of the supersaturation time derivative and the condensation term, and ii) the covariance, eq. (12), of the supersaturation and the intermittency of the small-scale, as represented by the fluctuations of the longitudinal derivatives of the velocities. In other words, we put

$$\frac{d\overline{S}}{dt} + \frac{\overline{S}}{\tau_{phase}} = \overline{\mathcal{P}_t} \sim \text{cov}_{S, \partial u_i / \partial x_i} \quad (21)$$

This is conceptually equivalent to modeling supersaturation production as the product of the supersaturation fluctuations and the characteristic frequency of small-scale turbulent structures, $\sim \tau_\eta^{-1}$, where the characteristic frequency of small-scale turbulent motions can be represented by the longitudinal velocity spatial derivatives.

The generation of small-scale anisotropy in turbulent shearless mixing has recently been investigated numerically. Data from direct numerical simulations for Taylor microscale Reynolds numbers between 45 and 150^{23–25,28,47} show that there is a significant departure of the longitudinal velocity derivative moments from the values found in homogeneous and isotropic turbulence and that the variation of skewness has the opposite sign for the components across the mixing layer and parallel to it. The anisotropy induced by the presence of a kinetic energy gradient has a very different pattern from the one generated by homogeneous shear. The transversal derivative moments in the mixing are in fact found to be very small, which highlights that smallness of the transversal moments is not a sufficient condition for isotropy. This intermittency is characterized by a large departure of the longitudinal derivative moments (as shown in Fig. 12 together with the supersaturation for two time instances), which are different in direction across and parallel to the layer from the typical values of the isotropic condition, even in such a flow, where there is no energy production (due to the lack of mean flow gradients). The structure of the anisotropy is such that the skewness departure from isotropy reduces the compression on the fluid filaments parallel to the mixing layer and enhances that of the filaments orthogonal to it.

The Pearson correlation coefficient, $\rho_{\overline{\mathcal{P}_t}, \text{cov}_{S, \partial u_i / \partial x_i}}$, inside the layer of thickness $\Delta(t)$, see eq. 14, was computed along the transient for $i=1,2,3$. The results are shown in Figure 13, where the data points have been collected for a time increment, that is approximately one half of the initial eddy turnover time.

When the correlation coefficient, that is, the linear correlation between two sets of data, is above 0.7, the correlation is defined as strong. However, we do not expect the numerical simulation to describe the first initial eddy turnover time of the transient accurately. The correlation coefficient

Supersaturation production and small-scale velocity statistics

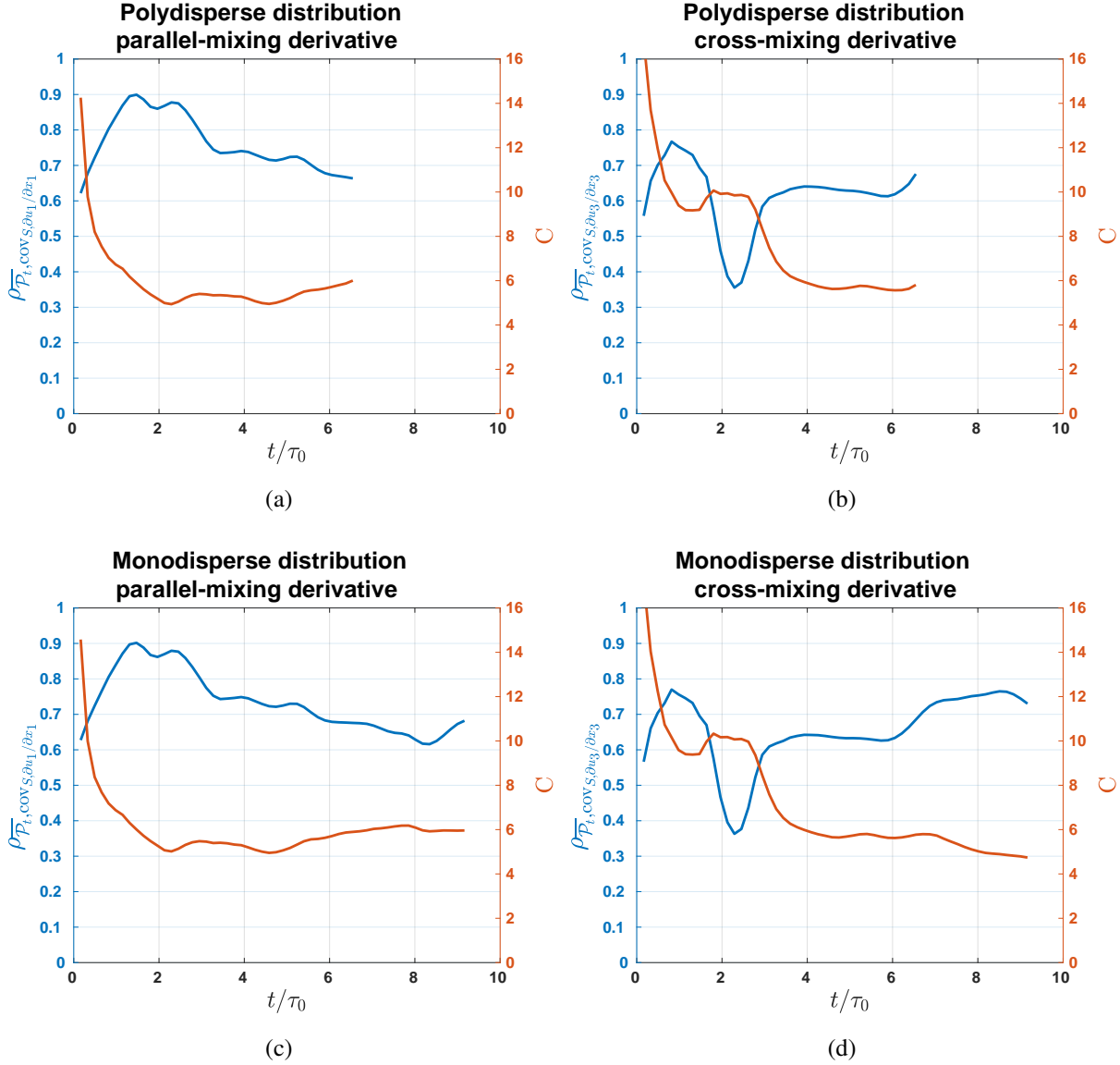


FIG. 13: Time evolution of the estimated production-planar covariance correlation coefficient and the proportionality constant. The Pearson correlation coefficient between the turbulence production term \mathcal{P}_t , see equation(21), and the supersaturation-velocity longitudinal derivative covariance (blue curves) plotted for the horizontal (left) and vertical (right) longitudinal derivatives during the transient. The correlation coefficient peaks around the first initial eddy turnover time and slowly decreases in magnitude to an asymptote ~ 0.7 as the transient progresses.

decreases slightly along the transient, beyond the first eddy turn over time, as the transient proceeds from values as high as 0.9, when the longitudinal velocity derivative is horizontal, and as high as 0.8, when the longitudinal velocity derivative is vertical, to values close to 0.7. This is true for

both monodisperse and polydisperse drop populations.

The relatively large absolute values of the correlation coefficients confirm that a quasi-linear relation should hold between the source term $\overline{\mathcal{P}}_t$ and $\text{cov}_{S\partial u_i/\partial x_i}$. An alternative way of estimating the proportionality constant, C , relevant to the dimensional quantities, along the transient is to integrate across the mixing layer of $\overline{\mathcal{P}}_t$ and $\text{cov}_{S\partial u_i/\partial x_i}$, $i = 1, 2$:

$$\int_{\Delta} \left| \frac{d\overline{S}}{dt} + \frac{\overline{S}}{\tau_{phase}} \right| dx_3 \cong C \int_{\Delta} |\text{cov}_{S\partial u_i/\partial x_i}| dx_3$$

The estimated values of the non-dimensional constant C are reported in Figure 13 (orange curve). Once again, the shape of the initial droplet size distribution does not seem to affect either the evolution of the correlation coefficient or the non-dimensional constant C during the transient. In all these cases, the estimated value is 5, an asymptotic value, that is rapidly reached after the first initial eddy turnover. We can observe a different pre-asymptotic trend for the horizontal and vertical longitudinal derivative correlation coefficients, which is due to the intrinsic small-scale anisotropy of the mixing layer between the cloudy region and the clear-air, see the discussion above.

IV. CONCLUSIONS

We have considered the relationship between supersaturation fluctuations and turbulent small-scale dynamics in the context of an inhomogeneous, anisotropic, shearless, turbulent air mixing layer, which is often used to model the carrier flow at the interface between warm clouds and unsaturated environmental air. Two initial droplet population types, that is, a $15\mu\text{m}$ -monodisperse one and constant-mass-per-volume-class polydisperse one, were tested.

The various time scales pertaining to the microphysics of a droplet population were compared inside the top of the cloudy region, the layer where the turbulent transport process toward the environmental subsaturated air takes place. The evaporation, reaction, and phase relaxation time scales match for a value close to $20 \sim 30$ s inside the layer just before the location where the supersaturation flux reaches its maximum rate of variation. In the case of a polydisperse population, this match includes the condensation time. The time scales before this spatial location are different, with differences of the order of one minute. Beyond this location, the evaporation and reaction times overlap, while the relaxation phase and condensation time scales asymptotically diverge, since the environment becomes more and more undersaturated.

Under the hypothesis of the supersaturation fluctuation depending to a great extent on the small-scale intermittency of the carrier flow that hosts the vapor and liquid water phases, we have analyzed the supersaturation balance equation with the aim of evincing their reciprocal correlation. In order to assess this hypothesis, we compared the estimated planar averages of the time derivative of the supersaturation and the condensation terms with the planar covariance of the supersaturation and the longitudinal velocity derivatives. The statistics of the velocity derivatives are in fact particularly relevant for small-scale dynamics. For the specific shearless turbulent structure considered

here, the longitudinal velocity derivatives are more significant for small-scale intermittency than the transversal ones, which are null. Moreover, the longitudinal velocity derivative can be considered as a characteristic measure of the small-scale frequency, τ_η^{-1} . We have found a high value of the Pearson correlation coefficient, $\rho_{\overline{\mathcal{P}_t}, \text{cov}_{S\partial u_i/\partial x_i}} \sim 0.7$ for the droplet populations, both inside the interfacial layer and along the entire simulation transient, which leads to the conclusion that, in the absence of an updraft, the mismatch of the time derivative of the supersaturation and the condensation terms is linearly related to the covariance of the supersaturation and the longitudinal velocity derivatives of the carrier flow.

ACKNOWLEDGEMENTS

This project has received funding from the Marie-Sklodowska Curie Actions (MSCA ITN ETN COMPLETE) under the European Union’s Horizon 2020 research and innovation program. Grant agreement 675675, <http://www.complete-h2020network.eu>.

We acknowledge Cineca - Supercomputer Applications and Innovations (SCAI) for providing the computational resources and technical support. All the runs were performed on the Marconi Tier-0 system from September 2019 to January 2020. The post-processing activity was in part conducted on the HACTAR cluster, and the computational resources were provided by HPC@POLITO, a project of Academic Computing within the Department of Control and Computer Engineering at the Politecnico di Torino (<http://www.hpc.polito.it>).

REFERENCES

- ¹J. Warner, “The microstructure of cumulus cloud. part i. general features of the droplet spectrum,” *Journal of Atmospheric Sciences* **26**, 1049–1059 (1969).
- ²J. Latham and R. L. Reed, “Laboratory studies of the effects of mixing on the evolution of cloud droplet spectra,” *Quarterly Journal of the Royal Meteorological Society* **103**, 297–306 (1977).
- ³M. B. Baker, R. G. Corbin, and J. Latham, “The influence of entrainment on the evolution of cloud droplet spectra: I. a model of inhomogeneous mixing,” *Quarterly Journal of the Royal Meteorological Society* **106**, 581–598 (1980).
- ⁴B. Kumar, J. Schumacher, and R. A. Shaw, “Cloud microphysical effects of turbulent mixing and entrainment,” *Theoretical and Computational Fluid Dynamics* **27**, 361–376 (2013).
- ⁵C. Lu, Y. Liu, B. Zhu, S. S. Yum, S. K. Krueger, Y. Qiu, S. Niu, and S. Luo, “On which microphysical time scales to use in studies of entrainment-mixing mechanisms in clouds,” *Journal of Geophysical Research: Atmospheres* **123**, 3740–3756 (2018).
- ⁶P. Squires, “The growth of cloud drops by condensation. i. general characteristics,” *Australian Journal of Chemistry* **5**, 59–86 (1952).
- ⁷R. Rogers and M. Yau, *A Short Course in Cloud Physics* (Elsevier Science, 1996).

- ⁸S. Twomey, “The nuclei of natural cloud formation part ii: The supersaturation in natural clouds and the variation of cloud droplet concentration,” *Geofisica pura e applicata* **43**, 243–249 (1959).
- ⁹M. K. Politovich and W. A. Cooper, “Variability of the supersaturation in cumulus clouds,” *Journal of the atmospheric sciences* **45**, 1651–1664 (1988).
- ¹⁰B. J. Devenish, P. Bartello, J.-L. Brenguier, L. R. Collins, W. W. Grabowski, R. H. A. IJzermans, S. P. Malinowski, M. W. Reeks, J. C. Vassilicos, L.-P. Wang, and Z. Warhaft, “Droplet growth in warm turbulent clouds,” *Quarterly Journal of the Royal Meteorological Society* **138**, 1401–1429 (2012).
- ¹¹W. W. Grabowski and L.-P. Wang, “Growth of cloud droplets in a turbulent environment,” *Annual Review of Fluid Mechanics* **45**, 293–324 (2013), <https://doi.org/10.1146/annurev-fluid-011212-140750>.
- ¹²W. A. Cooper, “Effects of variable droplet growth histories on droplet size distributions. part i: Theory,” *Journal of Atmospheric Sciences* **46**, 1301 – 1311 (1989).
- ¹³G. Sardina, F. Picano, L. Brandt, and R. Caballero, “Continuous growth of droplet size variance due to condensation in turbulent clouds,” *Phys. Rev. Lett.* **115**, 184501 (2015).
- ¹⁴K. K. Chandrakar, W. Cantrell, K. Chang, D. Ciochetto, D. Niedermeier, M. Ovchinnikov, R. A. Shaw, and F. Yang, “Aerosol indirect effect from turbulence-induced broadening of cloud-droplet size distributions,” *Proceedings of the National Academy of Sciences* **113**, 14243–14248 (2016).
- ¹⁵H. Siebert and R. A. Shaw, “Supersaturation fluctuations during the early stage of cumulus formation,” *Journal of the Atmospheric Sciences* **74**, 975–988 (2017).
- ¹⁶P. Prabhakaran, A. S. M. Shawon, G. Kinney, S. Thomas, W. Cantrell, and R. A. Shaw, “The role of turbulent fluctuations in aerosol activation and cloud formation,” *Proceedings of the National Academy of Sciences* **117**, 16831–16838 (2020).
- ¹⁷B. Kumar, J. Schumacher, and R. A. Shaw, “Lagrangian mixing dynamics at the cloudy–clear air interface,” *Journal of the Atmospheric Sciences* **71**, 2564–2580 (2014).
- ¹⁸Z. Gao, Y. Liu, X. Li, and C. Lu, “Investigation of turbulent entrainment-mixing processes with a new particle-resolved direct numerical simulation model,” *Journal of Geophysical Research: Atmospheres* **123**, 2194–2214 (2018).
- ¹⁹B. Kumar, P. Götzfried, N. Suresh, J. Schumacher, and R. A. Shaw, “Scale dependence of cloud microphysical response to turbulent entrainment and mixing,” *Journal of Advances in Modeling Earth Systems* **10**, 2777–2785 (2018).
- ²⁰R. S. Miller and J. Bellan, “Direct numerical simulation and subgrid analysis of a transitional droplet laden mixing layer,” *Physics of Fluids* **12**, 650–671 (2000).
- ²¹R. Onishi, K. Takahashi, and S. Komori, “Influence of gravity on collisions of monodispersed droplets in homogeneous isotropic turbulence,” *Physics of Fluids* **21**, 125108 (2009).
- ²²R. S. R. Sidin, R. H. A. IJzermans, and M. W. Reeks, “A lagrangian approach to droplet condensation in atmospheric clouds,” *Physics of Fluids* **21**, 106603 (2009).
- ²³M. Golshan, S. Abdunabiev, M. Tomatis, F. Fraternali, M. Vanni, and D. Tordella, “Intermit-

- tency acceleration of water droplet population dynamics inside the interfacial layer between cloudy and clear air environments,” *International Journal of Multiphase Flow* , 103669 (2021).
- ²⁴D. Tordella and M. Iovieno, “Small-scale anisotropy in turbulent shearless mixing,” *Phys. Rev. Lett.* **107**, 194501 (2011).
- ²⁵D. Tordella and M. Iovieno, “Decaying turbulence: What happens when the correlation length varies spatially in two adjacent zones,” *Physica D: Nonlinear Phenomena* **241**, 178 – 185 (2012), special Issue on Small Scale Turbulence.
- ²⁶D. Tordella, M. Iovieno, and P. R. Bailey, “Sufficient condition for Gaussian departure in turbulence,” *Phys. Rev. E* **77**, 016309 (2008).
- ²⁷D. Tordella and M. Iovieno, “Numerical experiments on the intermediate asymptotics of shear-free turbulent transport and diffusion,” *Journal of Fluid Mechanics* **549**, 429–441 (2006).
- ²⁸L. Gallana, S. Abdunabiev, M. Golshan, and D. Tordella, “Diffusion of turbulence following both stable and unstable step stratification perturbations,” arXiv preprint arXiv:2201.06920 (2022).
- ²⁹P. A. Vaillancourt, M. K. Yau, and W. W. Grabowski, “Microscopic approach to cloud droplet growth by condensation. part i: Model description and results without turbulence,” *Journal of the Atmospheric Sciences* **58**, 1945–1964 (2001).
- ³⁰M. Andrejczuk, W. W. Grabowski, S. P. Malinowski, and P. K. Smolarkiewicz, “Numerical simulation of cloud–clear air interfacial mixing,” *Journal of the Atmospheric Sciences* **61**, 1726–1739 (2004).
- ³¹P. Götzfried, B. Kumar, R. A. Shaw, and J. Schumacher, “Droplet dynamics and fine-scale structure in a shearless turbulent mixing layer with phase changes,” *Journal of Fluid Mechanics* **814**, 452–483 (2017).
- ³²D. Tritton, *Physical Fluid Dynamics*, Oxford Science Publ (Clarendon Press, 1988).
- ³³P. J. Ireland and L. R. Collins, “Direct numerical simulation of inertial particle entrainment in a shearless mixing layer,” *Journal of Fluid Mechanics* **704**, 301–332 (2012).
- ³⁴R. A. Shaw, “Particle-turbulence interactions in atmospheric clouds,” *Annual Review of Fluid Mechanics* **35**, 183–227 (2003).
- ³⁵K. K. Chandrakar, I. Saito, F. Yang, W. Cantrell, T. Gotoh, and R. A. Shaw, “Droplet size distributions in turbulent clouds: experimental evaluation of theoretical distributions,” *Quarterly Journal of the Royal Meteorological Society* **146**, 483–504 (2020).
- ³⁶S. J. Ghan, H. Abdul-Razzak, A. Nenes, Y. Ming, X. Liu, M. Ovchinnikov, B. Shipway, N. Meskhidze, J. Xu, and X. Shi, “Droplet nucleation: Physically-based parameterizations and comparative evaluation,” *Journal of Advances in Modeling Earth Systems* **3** (2011), 10.1029/2011MS000074.
- ³⁷H. Pruppacher and J. Klett, *Microphysics of Clouds and Precipitation*, Atmospheric and Oceanographic Sciences Library (Springer Netherlands, 2010).
- ³⁸R. Rogers, “Raindrop collision rate,” *Journal of the Atmospheric Sciences* **46**, 2469–72 (1989).
- ³⁹S. Balachandar and J. K. Eaton, “Turbulent dispersed multiphase flow,” *Annual Review of Fluid Mechanics* **42**, 111–133 (2010).
- ⁴⁰J. I. MacPherson and G. A. Isaac, “Turbulent characteristics of some canadian cumulus clouds,”

- Journal of Applied Meteorology **16**, 81–90 (1977).
- ⁴¹H. Siebert, K. Lehmann, and M. Wendisch, “Observations of small-scale turbulence and energy dissipation rates in the cloudy boundary layer,” *Journal of the Atmospheric Sciences* **63**, 1451–1466 (2006).
- ⁴²H. Siebert, R. A. Shaw, and Z. Warhaft, “Statistics of small-scale velocity fluctuations and internal intermittency in marine stratocumulus clouds,” *Journal of the Atmospheric Sciences* **67**, 262–273 (2010).
- ⁴³K. Lehmann, H. Siebert, and R. A. Shaw, “Homogeneous and inhomogeneous mixing in cumulus clouds: Dependence on local turbulence structure,” *Journal of the Atmospheric Sciences* **66**, 3641–3659 (2009).
- ⁴⁴H. Siebert, S. Gerashchenko, A. Gylfason, K. Lehmann, L. Collins, R. Shaw, and Z. Warhaft, “Towards understanding the role of turbulence on droplets in clouds: In situ and laboratory measurements,” *Atmospheric Research* **97**, 426–437 (2010), from the Lab to Models and Global Observations: Hans R. Pruppacher and Cloud Physics.
- ⁴⁵S. B. Pope, *Turbulent Flows* (Cambridge University Press, 2000).
- ⁴⁶T. Ishihara, T. Gotoh, and Y. Kaneda, “Study of high-reynolds number isotropic turbulence by direct numerical simulation,” *Annual Review of Fluid Mechanics* **41**, 165–180 (2009).
- ⁴⁷M. Iovieno, S. Di Savino, L. Gallana, and D. Tordella, “Mixing of a passive scalar across a thin shearless layer: concentration of intermittency on the sides of the turbulent interface,” *Journal of Turbulence* **15**, 311–334 (2014).
- ⁴⁸S. Veeravalli and Z. Warhaft, “The shearless turbulence mixing layer,” *Journal of Fluid Mechanics* **207**, 191–229 (1989).
- ⁴⁹M. Iovieno, C. Cavazzoni, and D. Tordella, “A new technique for a parallel dealiased pseudospectral navier–stokes code,” *Computer Physics Communications* **141**, 365–374 (2001).
- ⁵⁰K. A. Brucker, J. C. Isaza, T. Vaithianathan, and L. R. Collins, “Efficient algorithm for simulating homogeneous turbulent shear flow without remeshing,” *Journal of Computational Physics* **225**, 20–32 (2007).
- ⁵¹L. Djenidi, M. Kamruzzaman, and R. Antonia, “Power-law exponent in the transition period of decay in grid turbulence,” *Journal of Fluid Mechanics* **779**, 544–555 (2015).
- ⁵²V. Khvorostyanov and J. Curry, *Thermodynamics, Kinetics, and Microphysics of Clouds* (Cambridge University Press, 2014).
- ⁵³M. Andrejczuk, W. W. Grabowski, S. P. Malinowski, and P. K. Smolarkiewicz, “Numerical simulation of cloud–clear air interfacial mixing: Homogeneous versus inhomogeneous mixing,” *Journal of the Atmospheric Sciences* **66**, 2493–2500 (2009).
- ⁵⁴B. Mason and C. Chien, “Cloud-droplet growth by condensation in cumulus,” *Quarterly Journal of the Royal Meteorological Society* **88**, 136–142 (1962).
- ⁵⁵X.-Y. Li, A. Brandenburg, G. Svensson, N. E. L. Haugen, B. Mehlig, and I. Rogachevskii, “Condensational and collisional growth of cloud droplets in a turbulent environment,” *JOURNAL OF THE ATMOSPHERIC SCIENCES* **77**, 337–353 (2020).
- ⁵⁶M. Andrejczuk, W. W. Grabowski, S. P. Malinowski, and P. K. Smolarkiewicz, “Numerical

- simulation of cloud–clear air interfacial mixing: Effects on cloud microphysics,” *Journal of the Atmospheric Sciences* **63**, 3204–3225 (2006).
- ⁵⁷F. Burnet and J.-L. Brenguier, “Observational study of the entrainment-mixing process in warm convective clouds,” *Journal of the Atmospheric Sciences* **64**, 1995–2011 (2007).
- ⁵⁸H. E. Gerber, G. M. Fricks, J. B. Jensen, and J. G. Hudson, “Entrainment, mixing, and microphysics in trade-wind cumulus,” *Journal of the Meteorological Society of Japan. Ser. II* **86A**, 87–106 (2008).
- ⁵⁹C. A. Jeffery, “Effect of condensation and evaporation on the viscous-convective subrange,” *Physics of Fluids* **13**, 713–722 (2001).
- ⁶⁰A. Khain, M. Pinsky, and L. Magaritz-Ronen, “Physical interpretation of mixing diagrams,” *Journal of Geophysical Research: Atmospheres* **123**, 529–542 (2018).
- ⁶¹A. Monin and A. Yaglom, *Statistical Fluid Mechanics, Volume II: Mechanics of Turbulence*, Dover Books on Physics (Dover Publications, 2013).
- ⁶²R. Rogallo, “Numerical experiments in homogeneous turbulence,” Tech. Rep. (Advisory Group for Aerospace Research and Development, NASA Ames Research Center Moffett Field, CA, United States, 1981).
- ⁶³X. Shen and Z. Warhaft, “The anisotropy of the small scale structure in high reynolds number ($R_\lambda \sim 1000$) turbulent shear flow,” *Physics of Fluids* **12**, 2976–2989 (2000).
- ⁶⁴H. Tennekes and J. Lumley, *A First Course in Turbulence*, MIT Press (Pe Men Book Company, 1972).
- ⁶⁵Z. Warhaft, “Laboratory studies of droplets in turbulence: towards understanding the formation of clouds,” *Fluid Dynamics Research* **41**, 011201 (2008).
- ⁶⁶A. Wray, “Hom02: Decaying isotropic turbulence,” Tech. Rep. (Advisory Group for Aerospace Research and Development, 1998).
- ⁶⁷F. Yang, R. Shaw, and H. Xue, “Conditions for super-adiabatic droplet growth after entrainment mixing,” *Atmospheric Chemistry and Physics* **16**, 9421–9433 (2016).
- ⁶⁸S. S. Yum, J. Wang, Y. Liu, G. Senum, S. Springston, R. McGraw, and J. M. Yeom, “Cloud microphysical relationships and their implication on entrainment and mixing mechanism for the stratocumulus clouds measured during the vocals project,” *Journal of Geophysical Research: Atmospheres* **120**, 5047–5069 (2015).